International Journal for Uncertainty Quantification, 2 (3): 295–321 (2012)

SENSITIVITY ANALYSIS FOR THE OPTIMIZATION OF RADIOFREQUENCY ABLATION IN THE PRESENCE OF MATERIAL PARAMETER UNCERTAINTY

Inga Altrogge,[1] Tobias Preusser,[2,3] Tim Kröger,[4] Sabrina Haase,[3] Torben Pätz,[2,3] & Robert M. Kirby[5,*]

[1] *Center of Complex Systems and Visualization, University of Bremen, Germany*

[2] *School of Engineering and Science, Jacobs University Bremen, Germany*

[3] *Fraunhofer Institute for Medical Image Computing MEVIS, Bremen, Germany*

[4] *Georg Simon Ohm University of Applied Sciences, Nuremberg, Germany*

[5] *School of Computing, The University of Utah, Salt Lake City, Utah 84112, USA*

Original Manuscript Submitted: 30/09/2011; Final Draft Received: 6/01/2012

We present a sensitivity analysis of the optimization of the probe placement in radiofrequency (RF) ablation which takes the uncertainty associated with biophysical tissue properties (electrical and thermal conductivity) into account. Our forward simulation of RF ablation is based upon a system of partial differential equations (PDEs) that describe the electric potential of the probe and the steady state of the induced heat. The probe placement is optimized by minimizing a temperature-based objective function such that the volume of destroyed tumor tissue is maximized. The resulting optimality system is solved with a multilevel gradient descent approach. By evaluating the corresponding optimality system for certain realizations of tissue parameters (i.e., at certain, well-chosen points in the stochastic space) the sensitivity of the system can be analyzed with respect to variations in the tissue parameters. For the interpolation in the stochastic space we use an adaptive sparse grid collocation (ASGC) approach presented by Ma and Zabaras. We underscore the significance of the approach by applying the optimization to CT data obtained from a real RF ablation case.

KEY WORDS: *stochastic sensitivity analysis, stochastic partial differential equations, adaptive sparse grid, heat transfer, multiscale modeling, representation of uncertainty.*

1. INTRODUCTION

The interstitial thermal destruction of lesions with radiofrequency (RF) ablation has become a widely used technique for the treatment of tumor diseases in various organs. This work concentrates on the RF ablation of lesions in the liver. In RF ablation, a probe containing some electrodes which is connected to an electric generator is placed in the malignant tissue. Upon turning on the generator, the tissue is heated by an electric current due to its Ohm resistance. The heat causes the coagulation of proteins and consequently tissue cells die. The treatment is considered successful if all malignant cells are completely destroyed including a safety margin of about 0.5–1 cm (cf., e.g., [1]).

The success of an RF ablation treatment depends heavily on the anatomical configuration and on the experience of the attending medical doctor. As blood vessels in the vicinity of the lesion transport away the heat which is generated by the electric current, there is the risk that tumor cells close to blood vessels are not destroyed. As a consequence, local recurrences may result, and indeed there are recurrence rates of up to 60% reported in the literature [2]. At present, it mostly depends on the experience of the attending radiologist, surgeon, or gastroenterologist to select the

*Correspond to Robert M. Kirby, E-mail: kirby@cs.utah.edu, URL: http://www.cs.utah.edu/˜kirby

2152–5080/12/$35.00

therapy parameters, i.e., the placement of the probe and the settings of the electric generator such that the local blood flow does not hinder the success of the therapy.

These expositions motivated many medical scientists during the last decade to investigate RF ablation scenarios using mathematical modeling, simulation, and optimization. The common goal is to understand the biophysical processes involved in this treatment form and to allow for the planning of an optimal treatment for an individual patient in advance which would yield the greatest therapy quality and success.

The mathematical/biophysical models of this scenario which have been developed so far result in systems of partial differential equations (PDEs) [3–6]. These systems of PDEs allow for the numerical simulation of RF ablation yielding a prediction of the outcome for a given placement of the probe and power of the generator. Clearly, these models depend on the physical properties of the tissue, i.e., their electrical and thermal properties such as electrical and thermal conductivity, heat capacity, density, and water content. The full complexity of the biophysical processes leads to a fully nonlinearly coupled system of PDEs and further algebraic equations for the states of the system, which is difficult to treat numerically [7].

The modeling of tissue properties poses a particular challenge because they depend on the current state of the tissue, e.g., the electrical conductivity depends on the temperature, the water content, and also on the grade of destruction of the tissue [3, 8, 9]. In the work presented here we consider a simplified version of the model, thus restricting the investigations to the steady state and tissue properties, which do not depend on temperature, water content, and coagulation state of the tissue.

Moreover, the tissue properties vary interindividually, and in fact they are not exactly known. Values used in simulations are, for example, often based on *ex vivo* experiments of animal tissue [3]. In addition, experimental measurements are always accompanied with a certain range of errors. Consequently, truly patient-specific models for RF ablation are not currently feasible, and the question arises whether results obtained through simulations can be used efficaciously in the clinical setting. In our view, the issue of patient specific models and simulations is in fact the most challenging task for mathematical modeling and simulation in medicine.

For practical purposes, more relevant than the simulation of RF ablation is the inverse problem of finding an optimal placement for the RF probe such that a given lesion is completely destroyed. This optimization problem has been investigated by the authors with thorough mathematical approaches that minimize certain objective functions [10, 11]. The role of the objective function is to measure the "quality" of a given probe placement; a quantification of quality provides insight into the deviation of the achieved temperature from a desired temperature. Clearly this involves the use of one of the aforementioned models for forward simulations of RF ablation.

We end up with a nonconvex PDE-constrained optimization problem for which we cannot expect the existence of a unique global minimum. A mathematical analysis of this optimization problem is extremely challenging and probably even unfeasible given its underlying complexity. Our numerical experiments show that the energy landscape has many local minima and that a delicate tuning of the numerical algorithm and the parameters and stopping criteria involved is necessary. From the perspective of the medical application, however, this is not a drawback: For the medical doctor it is not relevant whether an optimal probe placement is unique or not. From their perspective, what is important is whether a proposed optimal placement can be incorporated in practice, whether it conflicts with other constraints of the therapy or the patient's case and—most importantly—how robust the therapy success is with respect to variations in the configuration and deviations in the actual practical probe placement.

In this paper we make first steps toward combining the optimization of the probe placement with the analysis of the uncertainty that is associated with material parameters, i.e., we investigate the sensitivity of the optimal probe placement with respect to variations in the material parameters. Thus, we do not consider the electric and thermal conductivity to have fixed values, but to be probabilistically distributed. The ranges for these parameters can be taken from experiments which are documented in the literature, or estimations of the measurement error can be taken into account. Substituting the probabilistically distributed values into the PDE model for the simulation of RF ablation yields a system of stochastic partial differential equations (SPDEs).

The goal of our investigations is to sensitize the attending medical doctor of the uncertainties associated with the optimal probe placement and thus reveal the robustness of a therapy plan with respect to the intrinsic patient-specific biological and anatomical variations, which cannot be quantified exactly. Using our results, it would be the task of the medical doctor to adjust the therapy plan (use multiple probes, different generator settings, or even a different

type of treatment) if the sensitivity analysis would show a possibly huge variation of the best probe placement, i.e., a nonrobust optimal placement, and thus a low confidence that the therapy can be performed with greatest success.

There are several different methods to discretize the stochastic component of this system. Probably the most popular approach is the (rather slowly converging) Monte Carlo simulation, which is a nonintrusive sampling methodology that requires a large number of randomly chosen sampling points to completely cover the stochastic space. We have instead elected to follow in the footsteps of the stochastic finite element framework advocated by Ghanem and Spanos [12] and subsequent refinements and additions of this seminal work for the discretization of the stochastic system arising in this problem. In the Related Work subsection below, we will situate the variants of the methodologies that we have employed in the context of what has already been proposed theoretically and demonstrated in the context of other uncertainty quantification problems. For the purposes of the current discussion, we merely note that we have elected to employ the adaptive sparse grid collocation method [13] (a modification of the global spectral finite element method that combines the power of collocating methods with the some of the theoretical properties of the *generalized polynomial chaos* framework [14]).

By evaluating the SPDE system for certain realizations of the material parameters in a collocating sense, we can analyze the sensitivity of the system with respect to variations in the coefficients of the PDE system, i.e., with respect to variations in the material parameters. To compute this sensitivity analysis we use the above mentioned adaptive sparse grid collocation (ASGC) Method with piecewise multilinear ansatz functions for the adaptive interpolation of the stochastic space. A mathematical analysis of the smoothness of our coupled SPDE system with respect to the stochastic parametrization (in the manner as described, e.g., in [15]) is very difficult or rather impossible due to the high complexity of our problem. Hence, although other methodologies that stem from the original work of Ghanen and Spanos may provide superior convergence properties under the assumption of sufficient smoothness within the stochastic space (e.g., polynomial collocation methods of [16]), we decided to employ the ASGC methodology with the understanding that it provided reasonable convergence rates (superior to Monte Carlo) while providing relative robustness in the presence of possible irregularities in the stochastic domain. In an empirical study of this sort with realistic medical data, this trade-off between theoretical convergence and robustness is very important to the practitioner.

1.1 Related Work

The numerical simulation of RF ablation (and related thermal therapies) has been considered by many authors [3, 4, 6, 17, 18]. A particular focus has been emphasized concerning the modeling of blood flow and its effect on the temperature distribution during RF ablation [5, 17, 19]. The optimization of the probe placement through a minimization of the L^2 distance between the achieved temperature and a critical temperature inside the tumor was first considered by the authors in [10]. A modification of our optimization that uses shape derivatives instead of central differences for the calculation of the descent direction in order to increase the robustness (i.e., the starting point independency) of our optimization algorithm will be published in [11]. In [20] Villard et al. approximate the complicated optimization with PDE constraints by a simple geometric optimization which uses templates for the elliptical shapes of temperature isosurfaces generated by RF probes. Butz et al. [21], who focus on the optimization of cryotherapy, but consider RF ablation as well, also use ellipsoidal approximations of the ablation zone, which they have obtained from the literature and additional experiments. Moreover, a related form of therapy (interstitial ultrasound) has been optimized in [22]. In [23] Seitel et al. present a trajectory planning system for percutaneous insertions that extends the work of Villard and Baegert [1, 24] and determines rated possible insertion zones/trajectories via hard and soft constraints using the concept of pareto optimality. However, here the ablated tissue region and its coverage of the tumor seems not to be under consideration (i.e., part of the soft constraints) any more. Kapoor et al. [25] formulate the task of optimizing the number and placement of multiple RF needle probes as mixed variable optimization problem with hard and soft constraints, which they solve with a derivative-free class of algorithms called mixed variable mesh adaptive direct search. In contrast to Seitel, et al. [23], they take into account the optimal thermal ablation coverage, but again use ellipsoidal-shaped approximations of single probe ablation zones, which are then combined with the resulting necrosis. In particular, they do not take into account the cooling effect of large blood vessels close by the tumor. In [26] Chen et al. optimize the RF probe's insertion depth and orientation under the assumption of a given,

fixed entry point of the probe. They use an objective function that depends on the survival fraction, which is predicted by a finite element computation of the Arrhenius formalism, but which is also approximated as a field that transforms rigidly with the electrode during the optimization. To the best of our knowledge none of the above approaches considers the uncertainty that is associated with tissue parameters due to their patient- and state dependence, as well as due to measurement errors.

The main stochastic theoretical underpinning of this work is generally referred to as *generalized polynomial chaos*. Based upon the Wiener-Hermite polynomial chaos expansion [27] and combined with finite elements in the global stochastic finite element method (GSFEM) of Ghanem and Spanos [12], generalized polynomial chaos seeks to approximate second-order random processes by a finite linear combination of stochastic basis functions which are global in nature. Once one has chosen an approximation space of the random process of interest, a solution within that space can be found by solving the stochastic partial differential system of interest in the weak form. Because of its analogy with the classic Galerkin method as employed in finite elements, this methodology is often referred to as the generalized polynomial chaos-stochastic Galerkin method (gPC-SG) [14]. It has been applied as a method for uncertainty quantification in the field of computational mechanics for a number of years and has recently seen a revival of interest [28–35]. This approach has also been applied successfully within the biological modeling world. In [36], Geneser et al. employed the gPC-SG approach to evaluate the effects of variations and uncertainty in the conductivity values assigned to organs in a two-dimensional electrocardiograph simulation of the human thorax.

Although the stochastic Galerkin method provides a solid mathematical framework from which one can do analysis and can derive algorithms, it is not always the most computationally efficient means of solving large problems. Nor is it the case that one always has the freedom to rearchitect their currently available deterministic solver to employ gPC-SG. To address these issues, nonintrusive combinations of stochastic Galerkin and Monte Carlo methods that decouple computations through the choice of interpolating basis have been developed [14].

For the sensitivity analysis of our optimization with respect to changes in the tissue parameters, we use a stochastic (collocating) finite element approach advocated by Ma and Zabaras called the adaptive sparse grid method (ASGM) (see [13, 37–39]). Within the gPC literature, this is sometimes referred to as multielement generalized polynomial chaos method (MEgPC) [40, 41]. In [13], a nice delineation and comparison of these methods in the historical context is provided; we recommend that the reader the introduction of that work for a more complete exposition on the interconnection between the various methods.

The optimization problem considered in this paper lies in the field of nonlinear optimization subject to infinite dimensional constraints given by a system of (stochastic) partial differential equations. For an overview of the methodology we refer the reader to [42]. The consideration of uncertainty in inverse problems and optimization problems with PDE constraints has not yet received much attention in the community. The estimation of parameters in the presence of noisy measurements has been treated with the Bayesian inference approach, which uses known information about the parameters to create *a priori* distribution [43–45]. A first approach to stochastic inverse problems is presented by Narayanan and Zabaras in [46], where the solution of the stochastic inverse heat equation is obtained with the method of polynomial chaos.

Gunzburger et al. analyze an SPDE-constrained stochastic Neumann boundary control problem in [47]. They prove the existence of an optimal solution and of a corresponding Lagrange multiplier and estimate the error for the finite element solution of the optimality system. Finally, Hou et al. [48] investigate an optimal control problem constrained by elliptic SPDEs, where the expectation of a tracking cost functional is considered. Again, the existence of an optimal solution and Lagrange multiplier is proven and moreover error estimates for the discretization of the probability space and for the finite element discretization of the spatial space are derived. A stochastic collocation approach to the solution of optimal control problems with stochastic PDE constraints is presented in [49]. In this work the authors derive a gradient descent method as well as a sequential quadratic program for the minimization of objective functions of tracking type, which involve stochastic moments of the state variables.

1.2 Paper Organization

The paper is organized as follows: In Section 2.1 we review the deterministic model used for the simulation of the electric potential and the temperature profile during RF ablation. We discuss the uncertainty of tissue properties, which

come into the PDE model as parameters in Section 2.2. Consequently we extend the deterministic PDE model toward a stochastic PDE (SPDE) model taking into account stochastically distributed parameters and states. In Section 2.3 a review of the optimization of the probe placement will be given including a description of the objective function, a multiscale gradient descent approach for its minimization as well as our approach to the analysis of the sensitivity of the optimal probe placement. Section 2.4 is devoted to the discretization of the stochastic PDE model and the optimization with a composite finite element (CFE) approach in the physical space and the adaptive sparse grid collocation (ASGC) method in the stochastic dimensions. We show results and different sensitivity analyses based on a true RF ablation case and corresponding segmented CT data in Section 3. Finally we draw conclusions in Section 4.

2. SIMULATION AND OPTIMIZATION OF RF ABLATION

In this section we present a PDE model for the simulation of the RF ablation and for the optimization of the probe placement. The model is parametrized by a set of biophysical parameters which characterize the electric and thermal conductivity of the tissue under treatment. We will discuss the uncertainty associated with the values of these parameters and discuss how to incorporate them into an analogous system of stochastic PDEs. The actual optimization of the probe placement is discussed as well as the analysis of the sensitivity of the optimal placement with respect to variations in the material parameters.

We consider the computational domain to be a cuboid $D \subset \mathbb{R}^3$ in the three-dimensional space with boundary $B = \partial D$ in which a tumor $D_{\mathrm{t}} \subset D$ and vascular structures $D_{\mathrm{v}} \subset D$ are located. Furthermore, we assume that a monopolar RF probe is applied in D, whose position $p \in D$ (of the active zone's center) and direction $a \in S^2 = \{x \in \mathbb{R}^3 : |x| = 1\}$ are variables (over which we would like to optimize later). The subset of D that is covered by the probe is denoted by D_{pr}, and the subset covered by the electrode is denoted by D_{el} (cf. Fig. 1). Note that these sets depend on p and a. In practical applications the sets D_{t} and D_{v} are determined from segmented image data in advance, e.g., by the methods presented in [50]. Moreover, to achieve the desired safety margin we can consider D_{t} to be a dilated version of the original segmented tumor mask.

2.1 Deterministic Simulation of RF Ablation

Let us first describe how to compute the heat distribution in the tissue D for a fixed position and orientation of the probe, that is, for fixed D_{pr} and D_{el}. Note that here we work with a reduced and simplified model; for details on the full model of RF ablation we refer the reader to [7].

The forward simulation model consists of two parts. The first component is the electrostatic equation that describes the electric potential of the tissue which is induced by the electric potential of the electrodes. The second component

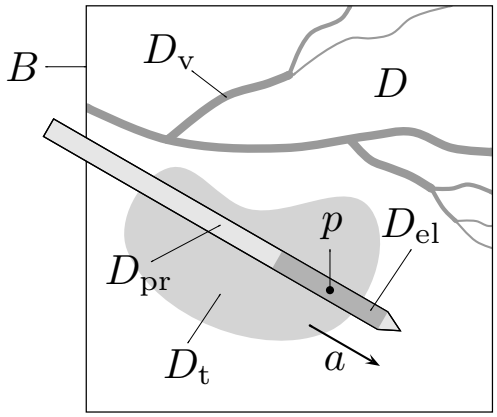

FIG. 1: Schematic sketch of the considered configuration identifying the different geometric regions specified in the text. Note that $D_{\mathrm{el}} \subset D_{\mathrm{pr}}$ where both sets depend on p and a.

is the heat equation which models the distribution of temperature once the heat source from the electric potential is known.

The electric potential $\phi : D \to \mathbb{R}$ of the RF probe is modeled by the *electrostatic equation*

$$-\mathrm{div}[\sigma(x)\nabla\phi(x)] = 0 \qquad \text{in } D \setminus \overline{D_{\mathrm{el}}}, \tag{1}$$

with appropriate boundary conditions (see below). Here, $\sigma : D \to \mathbb{R}$ is the electric conductivity of the tissue. It is known that the electric conductivity also depends on the temperature, the water content, and the protein state of the tissue. More refined models for the forward simulation take this behavior into account [7, 51]. However, since our approach is a first step towards an optimization of the probe placement (i.e., the inverse problem), we do not consider this dependence and merely investigate the spatial variation of $\sigma = \sigma(x)$. For the electrostatic equation (1) we consider the inner boundary condition

$$\phi = 1 \qquad \text{on } \overline{D_{\mathrm{el}}}\ , \tag{2a}$$

which fixes the potential on the electrode; below, we are going to scale the heat source resulting from the electric field according to the actual voltage which is imposed by the generator. Furthermore, as outer boundary conditions for (1) we consider the Dirichlet boundary condition

$$\phi = 0 \qquad \text{on } B\ . \tag{2b}$$

Due to the electric resistance of the tissue, the potential ϕ induces a heat source Q_{RF}. However, the magnitude of this heat source depends on the power of the generator and the impedance (resistance) of the tissue, which leads to a decreased energy input if the impedance increases. To model this dependence on the characteristics of the generator, we take the equivalent circuit diagram shown in Fig. 2 into account [3]. This yields a characteristic curve of the generator of the type presented in Fig. 2. The curve shows that depending on the resistance of the tissue the effective power applied to the tissue is in general smaller than the maximum power of the generator.

To provide the reader with a better perspective on how this nonlinear relationship impacts the system, we provide more details on the coupling: The impedance R of the tissue is given by

$$R = \frac{U^2}{P_{\mathrm{total}}} \quad \text{with} \quad P_{\mathrm{total}} = \int_D \sigma|\nabla\phi|^2\,dx, \tag{3}$$

where $U = 1\,\mathrm{V}$ is the potential ϕ of the electrode [cf. (2a)]. According to the equivalent circuit diagram shown in Fig. 2, the effective power of the generator is now given by

$$P_{\mathrm{eff}} = \frac{4P_{\mathrm{setup}}RR_{\mathrm{I}}}{(R+R_{\mathrm{I}})^2}, \tag{4}$$

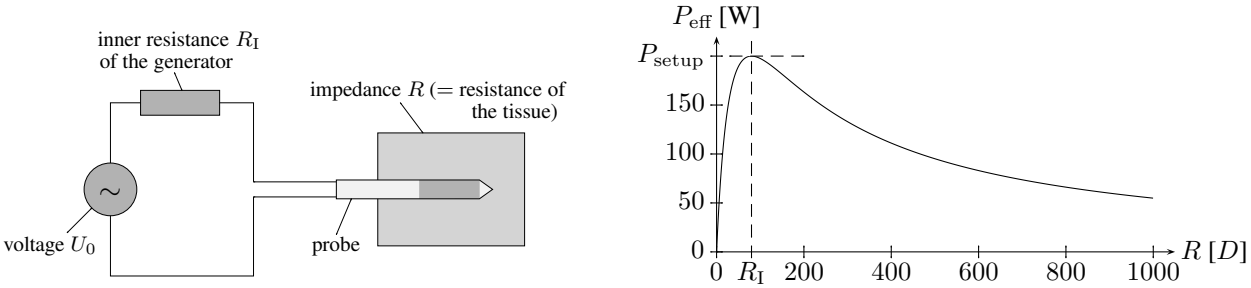

FIG. 2: Left: Equivalent circuit diagram for the calculation of the scaling factor which is needed to convert the unscaled power P into the effective heat source Q_{RF}. Right: The characteristic curve of the generator shows the dependence of the effective power P_{eff} on the impedance R of the tissue, while R_{I} and P_{setup} are fixed (here: $R_{\mathrm{I}} = 80\,\Omega$, $P_{\mathrm{setup}} = 200\,\mathrm{W}$).

where R_{I} is the inner resistance of the generator and P_{setup} is the value setup at the generator's control unit. Finally, the heat source is given by

$$Q_{\mathrm{RF}}(x) = \frac{P_{\mathrm{eff}}}{P_{\mathrm{total}}}\, \sigma(x)|\nabla\phi(x)|^2 \qquad \text{in } D, \tag{5}$$

which is proportional to the square of the magnitude of the electric field $\nabla\phi$ imposed by the electric potential ϕ.

The heat distribution $T : D \to \mathbb{R}$ is modeled by the steady state of the *bioheat-transfer equation*

$$-\mathrm{div}[\lambda(x)\nabla T(x)] = Q_{\mathrm{RF}}(x) + Q_{\mathrm{perf}}(x) \qquad \text{in } D. \tag{6}$$

Here, $\lambda : D \to \mathbb{R}$ is the thermal conductivity of the tissue. Again in our first step toward optimization, we only take spatial variation of the heat conductivity into account. More refined models also consider the dynamics of the heat distribution and the dependence of λ on other states (water content, protein state) of the system [7].

Known values of the electric conductivity σ and of the thermal conductivity λ for the above model are based mostly on experiments performed on, e.g., animal tissue or cadaveric human tissue. The fact that this kind of tissue has different electric and thermal properties than native liver tissue as well as the associated experimental measurement errors are the sources for the parameter uncertainty that are investigated in this work.

The right-hand side of (6) consists of the source (heating) Q_{RF} due to the electric current and the sink (cooling) Q_{perf} due to the blood flow in the vascular structures D_{v}. We assume that there is no heating on the outer boundary of D, i.e., we choose D to be sufficiently large (cf. also Section 3). Thus, we consider the Dirichlet boundary condition

$$T = T_{\mathrm{body}} \qquad \text{on } B. \tag{7}$$

To model the cooling effects of the blood perfusion, we use a weighted variant of the approach of Pennes [52]:

$$Q_{\mathrm{perf}}(x) = -\nu(x)\,[T(x) - T_{\mathrm{body}}], \qquad \nu(x) = \begin{cases} \nu_{\text{vessel}}\ \rho_{\text{blood}}\ c_{\text{blood}}, & \text{if } x \in D_{\mathrm{v}}, \\ \nu_{\text{cap}}\ \rho_{\text{blood}}\ c_{\text{blood}}, & \text{else.} \end{cases} \tag{8}$$

Thus, the coefficient $\nu : D \to \mathbb{R}$ depends on the relative blood circulation rate ν_{vessel} $[\mathrm{s}^{-1}]$ of vessels and ν_{cap} $[\mathrm{s}^{-1}]$ of capillaries, respectively, as well as on the blood density ρ_{blood} $[\mathrm{kg/m}]$ and the heat capacity c_{blood} $[\mathrm{J/kg\ K}]$ of blood. Here, we assume that the whole tissue is pervaded by capillary vessels and thus is exposed to their cooling influence. For simplicity, the coefficient ν_{cap} is also assumed on the probe, i.e., within D_{pr} and D_{el}. We emphasize that for the modeling of blood flow we have again purposely chosen a very simple approach.

Remark

The modeling of perfusion has been investigated by many authors [53–57]. Sheu et al. [58] investigate the influence of different heat transfer coefficients between tissue and vessels. These authors conclude that with increasing ablation time, the relative influence of cooling through blood advection decreases, whereas the capillary/diffusive cooling increases. Obviously, the unknown heat transfer coefficients between tissue and blood flow pose another important source of uncertainty in the simulation of RF ablation. We emphasize that the stochastic finite element method is capable of handling these uncertain heat transfer coefficients in the bioheat transfer equation. However, in the present work we did not investigate this uncertainty. We also note that taking into account uncertainty in flow simulations with, e.g., the Navier-Stokes equations, is a more involved topic which has been investigated in, e.g., [35].

Remark

In the literature it is common to estimate the damage inflicted to the tissue through the temperature profile by the Arrhenius formalism [59]. This formalism considers a history integral over a certain function of the temperature, thus it takes into account that already at low temperatures (in the range of a high fever, i.e., $T \gtrsim 43^{\circ}\mathrm{C}$) destruction of tumor cells takes place. A different approach considers a critical temperature, i.e., the temperature at which (according to the Arrhenius formalism) the tissue is destroyed after an exposure time of $1\,\mathrm{s}$. Clearly, using this approach is much simpler; however the size of lesions is underestimated.

In summary, the states $\phi : D \to \mathbb{R}$ and $T : D \to \mathbb{R}$ are defined by the boundary value problems

$$-\mathrm{div}[\sigma(x)\nabla\phi(x)] = 0 \qquad \text{in } D \setminus \overline{D_{\mathrm{el}}}, \tag{9a}$$

$$-\text{div}[\lambda(x)\nabla T(x)]+\nu(x)T(x) = Q_{\text{RF}}(x)+\nu(x)T_{\text{body}} \qquad \text{in } D, \tag{9b}$$

with boundary conditions (2) and (7). Note that the two equations are coupled through the term Q_{RF}.

2.2 Parameter Uncertainty

The PDE model for the simulation of the heat distribution described in the last section involves the electric and thermal conductivity of the corresponding tissue. As we have discussed in the Introduction, these quantities cannot be determined exactly. The material properties depend on the physical state of the tissue, and moreover they vary interindividually (i.e., from patient to patient) and in fact they also vary from day to day depending on the patient's physical constitution. The range of values, which is given in the literature, underlines this uncertainty, e.g., from [3, 4, 6, 9] we learn that even in native liver tissue we have

$$\sigma = 0.17 \text{ S/m—}0.60 \text{ S/m}, \qquad \lambda = 0.47 \text{ W/Km—}0.64 \text{ W/Km}. \tag{10}$$

These values have mostly been obtained from *in vitro* experiments on cadaveric human tissue or animals, and they are certainly furthermore associated with realistic measurement errors of 10% or more.

Taking the uncertainty of the values of material parameters into account leads to the question about the dependence of the forward simulation of RF ablation and also about the sensitivity of the optimal probe placement (see Section 2.3) with respect to variations (either due to uncertainty or errors) in the material parameters. Discussing this question does not improve the accuracy of the simulation or the optimization (as numerical verification is a matter divorced from the answer to this question); rather, it enables us to quantify how the uncertainty of the electric and thermal conductivities affects (or propagates through) the numerical results. Based on the results obtained by our sensitivity analysis, a future goal is in the direction of patient-specific modeling and simulation whereby we will (hopefully) be able to optimize the confidence of the success of the therapy.

In the following, we extend the model for the simulation of RF ablation presented in Section 2.1 such that it incorporates the uncertainty in the material properties. We present a review of the optimization of the probe placement and discuss different variants to analyze the sensitivity of the optimal probe placement in Section 2.3. In Section 2.4 we review the adaptive sparse grid collocation method, which we use in this work.

Let $(\Omega, \mathcal{A}, \mu)$ be a probability space expressing the behavior of the thermal conductivity and electric conductivity where Ω is the event space, $\mathcal{A} \subset 2^{\Omega}$ the σ-algebra, and μ the probability measure. In the following we consider the case that the tissue parameters σ and λ are not fixed to particular (deterministic) values, but rather lie within a range of possible values. Thus, an event ω in our probability space consists of a particular choice of the material properties (σ, λ). The physical parameters can be considered as random fields expressible in terms of random variables and characterizable by their probability density functions (PDFs).

For the medical problem of interest, let us assume that we have three main types of tissue present in our computational domain: native liver tissue (n), tumor tissue (t), and blood vessels (v). For each of these tissue types we assume that the distributions of σ and λ are controlled by uniformly distributed independent random variables.

Following [14], we know that we can represent any general second-order *random process* $g(\omega)$, $\omega \in \Omega$ in terms of a collection of random variables $\boldsymbol{\xi} = (\xi_1, \ldots \xi_N)$ with independent components up to some truncation error. For certain processes and choices of basis functions, this truncation error can be shown to be zero given particular values of N. In general, as with spectral methods, we rely on the fact that if the process is smooth, given sufficiently large N the size of this truncation error will be small. Ideally, one would attempt to provide bounds on the magnitude of this term; for our optimization problem, the magnitude of this truncation error is very difficult to quantify and can only indirectly be inferred by monitoring the convergence of our hierarchical collocated refinement scheme presented subsequently.

Here, the stochastic process under investigation is the optimal probe placement $\bar{u}$ as it is obtained by the algorithm that will be described in the next subsection. Since the optimal probe placement depends on the material parameters σ and λ, any uncertainty associated with those parameters will induce uncertainty in the optimal probe placement. Note that in the following we will also refer to *random fields* as stochastic processes.

Remark
Here and in the following we assume that the distributions for the three-different components of the material parameters are independent. Note that from the mathematical viewpoint it is very convenient to assume independence since it allows us to construct tensor-product Hilbert spaces on the stochastic domain. Note independence may not be justified from the anatomical perspective, since, e.g., the different conductivities are correlated through the water content of the tissue. However, there exists a mathematically rigorous (nonlinear) mapping which transforms a set of random variables into a set of independent random variables. This research falls into the area of numerical representation of non-Gaussian processes, which remains an active research field [16].

To describe the electric field emerging from the RF probe regarded as a random field, let us consider the vector of random variables $\xi^\sigma = (\xi_{\rm n}^\sigma, \xi_{\rm t}^\sigma, \xi_{\rm v}^\sigma) \in \Gamma_\sigma \subset \mathbb{R}^3$ (i.e., $N = 3$) which describes the uncertainty in the electric conductivity of the native tissue, the tumor, and the vessels. We model the stochastic field $\sigma(x, \xi^\sigma)$ for the uncertain electric conductivity by

$$\sigma(x,\xi^\sigma) = \begin{cases} \sigma_{\rm n}(\xi_{\rm n}^\sigma) & \text{if } x \in D_{\rm n}, \\ \sigma_{\rm t}(\xi_{\rm t}^\sigma) & \text{if } x \in D_{\rm t}, \\ \sigma_{\rm v}(\xi_{\rm v}^\sigma) & \text{if } x \in D_{\rm v}. \end{cases} \tag{11}$$

To model the uncertain distribution of heat we proceed similarly by considering $\xi^\lambda = (\xi_{\rm n}^\lambda, \xi_{\rm t}^\lambda, \xi_{\rm v}^\lambda) \in \Gamma_\lambda \subset \mathbb{R}^3$. The three components of ξ^λ represent the heat conductivity in the native and malignant tissue as well as in the vascular structures. As in (11) we define the overall heat conductivity $\lambda(x, \xi^\lambda)$. We will henceforth consider our input parameters to be of the form $\sigma(x, \xi^\sigma)$ and $\lambda(x, \xi^\lambda)$ given by $\xi = (\xi^\sigma, \xi^\lambda) \in \Gamma$ distributed over the ranges as, e.g., given in (10), where $\Gamma := \Gamma_\sigma \times \Gamma_\lambda \subset \mathbb{R}^3 \times \mathbb{R}^3$.

Having introduced the uncertain electric conductivity, we can formulate a *stochastic electrostatic equation* similar to (1) and (2): Find a stochastic field $\phi(x, \xi^\sigma)$ such that

$$\begin{aligned} -\mathrm{div}[\sigma(x,\xi^\sigma)\,\nabla\phi(x,\xi^\sigma)] = 0 \quad &\text{a.e. in } D \setminus \overline{D_{\rm el}} \times \Gamma_\sigma \ , \\ \phi(x,\xi^\sigma) = 1 \quad &\text{a.e. on } \overline{D_{\rm el}} \times \Gamma_\sigma \ , \\ \phi(x,\xi^\sigma) = 0 \quad &\text{a.e. on } \partial D \times \Gamma_\sigma \ . \end{aligned} \tag{12}$$

Straightforwardly, we can proceed to incorporate the uncertainty into the remaining components of the model that have been presented in Section 2.1. This yields a stochastic field for the heat source and stochastic processes for the total and the effective power, i.e.,

$$Q_{\rm RF}(x,\xi^\sigma) = \frac{P_{\rm eff}(\xi^\sigma)}{P_{\rm total}(\xi^\sigma)}\,\sigma(x,\xi^\sigma)|\nabla\phi(x,\xi^\sigma)|^2 \ , \tag{13}$$

$$P_{\rm eff}(\xi^\sigma) = \frac{4P_{\rm setup}R(\xi^\sigma)R_{\rm I}}{[R(\xi^\sigma)+R_{\rm I}]^2} \ , \quad R(\xi^\sigma) = \frac{U^2}{P_{\rm total}(\xi^\sigma)} \ , \quad P_{\rm total}(\xi^\sigma) = \int_D \sigma(x,\xi^\sigma)|\nabla\phi(x,\xi^\sigma)|^2\,dx \ . \tag{14}$$

We may also define the *stochastic heat equation* by analogy to (6) and (7). Since the source term on the right hand side depends on the solution of the stochastic electrostatic equation, the temperature distribution is going to be a random field that depends on both ξ^σ and ξ^λ, i.e.,

$$\begin{aligned} -\mathrm{div}[\lambda(x,\xi^\lambda)\nabla T(x,\xi)] = Q_{\rm RF}(x,\xi^\sigma) + Q_{\rm perf}(x,\xi) \quad &\text{a.e. in } D \times \Gamma, \\ T(x,\xi) = T_{\rm body} \quad &\text{a.e. on } \partial D \times \Gamma, \end{aligned} \tag{15}$$

where $\xi = (\xi^\sigma, \xi^\lambda)$. The sink term $Q_{\rm perf}$ in (15) is modeled as in Section 2.1

$$Q_{\rm perf}(x,\xi) = -\nu(x)\,[T(x,\xi) - T_{\rm body}], \qquad \nu(x) = \begin{cases} \nu_{\rm vessel}\ \rho_{\rm blood}\ c_{\rm blood} & \text{for } x \in D_{\rm v}, \\ \nu_{\rm cap}\ \rho_{\rm blood}\ c_{\rm blood} & \text{else.} \end{cases} \tag{16}$$

2.3 Optimizing the Probe Placement

The aim of the RF ablation therapy is the complete destruction of the lesion including a sufficiently large safety margin. Thus, for a given lesion it must be decided by the attending doctor how to place the RF probe such that this goal is achieved. In this section we review and extend an earlier work [10, 11], which uses mathematical optimization to find the best probe placement. Our exposition in this section is the basis for an analysis of the sensitivity of the optimization with respect to the uncertainty related to the material parameters.

2.3.1 Objective Function

In the following, we focus on an objective function which measures the "quality" of a given temperature distribution, i.e., which estimates the success that would be obtained with a given probe placement. For reasons of stability and robustness of the optimizer, we base our objective functional directly on the temperature profile. Thus, we relate our approach to the notion of critical temperature, having in mind that we (systematically) underestimate the size of lesions (see our remark above).

For the optimization we consider an optimal ablation result to be a maximum volume of destroyed tissue, which is obtained by high temperatures inside the lesion D_t. Thus, to maximize the volume of ablated tissue we would therefore want to maximize the lowest temperature inside the lesion including a safety margin. Since we do not aim at an optimization of the generator power P_setup, it does not make sense to directly consider the deviations from a critical temperature. In fact, the critical temperature would only change our chosen objective function by a constant term (see [11]).

To be more precise, let us remember that admissible probe parameters lie in the space $U := D \times S^2$. Thus, we aim at finding the optimal probe placement $(\bar{p}, \bar{a})$ such that

$$(\bar{p}, \bar{a}) = \operatorname*{argmax}_{(p,a)\in U} \min_{x\in D_\mathrm{t}} T(x) = \operatorname*{argmin}_{(p,a)\in U} \left(- \min_{x\in D_\mathrm{t}} T(x) \right) ,$$

where T depends on the probe placement (p, a). This objective is designed such that the smallest temperature that is attained inside the lesion is maximized. Since the $\min$-function is not differentiable it is popular to approximate it by a smooth function. In the following we use the approximation

$$\tilde{f}(T) := \frac{1}{\alpha} \log \left(\frac{1}{|D_\mathrm{t}|} \int_{D_\mathrm{t}} \exp \big[- \alpha T(x) \big] \, dx \right) \tag{17}$$

for some $\alpha > 0$. Note that for $\alpha \to \infty$, the integrand $\exp[-\alpha T(x)]$ converges to zero slowest for the smallest value of $T(x)$. Thus, for large α the integrand can be approximated by the constant value $\exp(-\alpha \min_{D_\mathrm{t}} T)$. Consequently for large α the integral reduces to $\alpha^{-1} \log[|D_\mathrm{t}|^{-1} \int_{D_\mathrm{t}} \exp(-\alpha \min_{D_\mathrm{t}} T) \, dx]$, and $\tilde{f}(T)$ simplifies to $- \min_{D_\mathrm{t}} T$.

With our choice of approximation (17), which uses the exponential function, we seek an equal heat distribution inside the tumor, since therewith the lowest temperature inside the tumor is penalized most. The factor $\alpha > 0$ models the grade of penalization of a nonuniform temperature distribution inside the tumor.

We can write $\tilde{f}(T) = K + \alpha^{-1} f(T)$ with $K = \alpha^{-1} \log(1/|D_\mathrm{t}|)$ and thus arrive at

$$f(T) := \log \left(\int_{D_\mathrm{t}} \exp \big[- \alpha T(x) \big] \, dx \right) , \tag{18}$$

which is a simpler objective function than $\tilde{f}$. Consequently our optimization problem becomes

$$(\bar{p}, \bar{a}) = \operatorname*{argmin}_{(p,a)\in U} f(T) = \operatorname*{argmin}_{(p,a)\in U} \log \left(\int_{D_\mathrm{t}} \exp \big[- \alpha T(x) \big] \, dx \right) . \tag{19}$$

Formally, our objective function f defined above is a function of the temperature distribution T. But T depends on the heat source Q_RF, and Q_RF depends on the optimization parameter $(p, a) =: u \in U$. We can handle these

dependencies by expressing our optimization problem as follows: we seek a positioning u such that the cost function given in terms of the positioning $F(u) = f \circ \mathcal{T} \circ \mathcal{Q}(u)$ is minimized, where

$$\mathcal{Q}(u) = Q_{\mathrm{RF}}, \quad T = \mathcal{T}(Q_{\mathrm{RF}}).$$

Obviously, in certain situations the uniqueness of a minimizing configuration is not guaranteed, e.g., for spherical tumors. This situation may also occur in practice for hepatic tumors, which in general have a spherical-like shape. However, such a symmetry is broken by the consideration of surrounding blood vessels and their cooling effects. Moreover, for practical reasons the uniqueness of a solution is not needed and even local minima give important information about good probe and generator configurations. In a future model we will incorporate constraints for the optimization parameters which break any existing symmetry even further. Such constraints are given by anatomical structures (bones, colon, diaphragm) that must not be punctured during the ablation.

2.3.2 Multiscale Gradient Descent

For the minimization of the objective functional F, we use a gradient descent method. Since the orientation a lies on the two-dimensional sphere S^2 and the computation of a gradient on the sphere would involve some difficulties (in particular because there is no basis of the tangent space of S^2 at a that depends continuously on a), we replace U by the open set

$$\tilde{U} = D \times (\mathbb{R}^3 \setminus \{0\}) \supset U,$$

and use in each step of the gradient descent method the projection

$$P_{D\times S^2} : \tilde{U} \to U, \qquad (p, a) \mapsto (p, a/|a|).$$

We also define a continuation of our solution operator $\mathcal{Q}$ onto $\tilde{U}$ that does not depend on the length of a via

$$\mathcal{Q}(p, a) = (\mathcal{Q} \circ P_{D\times S^2})(p, a) = \mathcal{Q}(p, a/|a|).$$

Letting the superscript $n \in \mathbb{N}$ denote the iteration count, we can describe the particular ingredients of our gradient descent method as follows:

- **Initial value.** Set $n = 0$, and choose an arbitrary probe positioning $u^0 \in U$ as an initial guess.
- **Descent direction.** Then, in each iteration step $n \geq 1$, calculate the descent direction $w^n \in \tilde{U}$ from the current iterate u^n as an approximation of $-D_u F(u^n) = -D_u[f \circ T \circ Q_{\mathrm{RF}}(u^n)] = -D_T f \cdot D_{Q_{\mathrm{RF}}} T \cdot D_u Q_{\mathrm{RF}}(u^n)$ (see Algorithm 1).
- **Step size.** Determine the step size $s^n > 0$, such that the resulting new iterate $u^{n+1} = P_{D\times S^2}(u^n + s^n w^n)$ is admissible, i.e., fulfills $u^{n+1} \in U$ and reduces the value of the objective function $F(u^{n+1}) < F(u^n)$. Using the projection $P_{D\times S^2}$, we assert that the new orientation lies on the sphere.
- **Stopping criterion.** The iteration continues until the difference $|u^{n+1} - u^n|$ falls below a given threshold θ.

To accelerate the gradient descent algorithm, we use a multiscale approach, i.e., we start with the optimization on a coarse grid and use the solution as the initial guess on a finer grid. In Algorithm 1 we show the complete multiscale optimization algorithm in pseudo-code. For each level l (see lines 3–25 of Algorithm 1) of the computational grid the optimization is performed as described above. The descent direction w^n in line 7 of Algorithm 1 is computed with help of a conjugate gradient calculation of the corresponding adjoint equation (see [10, 11]) and a determination of the derivative of the heat source Q_{RF} with respect to the probe positioning u via shape derivatives (see [11]). Specifically, we interpret the probe placement $u \in \tilde{U}$ as a vector of shape parameters $p \in \mathbb{R}^6$ such that the computational domain D depends on p, i.e., $D = D(p)$ and in particular $D_{\mathrm{el}} = D_{\mathrm{el}}(p)$. Then we can calculate $\partial_{p_i} Q_{\mathrm{RF}}$ as

$$\begin{aligned}\partial_{p_i} Q_{\mathrm{RF}} &= \partial_{p_i}\left(\frac{P_{\mathrm{eff}}}{P_{\mathrm{total}}}\,\sigma|\nabla\phi|^2\right)\\ &= \sigma\left[-2\int_D \sigma\nabla\phi\nabla(\partial_{p_i}\phi)dx\left(P_{\mathrm{eff}} + P_{\mathrm{eff}}\,\frac{R_{\mathrm{I}} - R}{R(R+R_{\mathrm{I}})}\,\frac{U^2}{P_{\mathrm{total}}}\right)\frac{|\nabla\phi|^2}{P_{\mathrm{total}}^2} + 2\,\frac{P_{\mathrm{eff}}}{P_{\mathrm{total}}}\,\nabla\phi\nabla(\partial_{p_i}\phi)\right].\end{aligned}$$

Algorithm 1 Multiscale gradient descent for the optimization of the probe placement

1: $l \leftarrow l_0$ ▷ Start with level l_0
2: Initialize $\bar{u}$.
3: **while** $l \leq L$ **do**
4: $u^0 \leftarrow \bar{u}$ ▷ Initialization
5: $n \leftarrow 0$
6: **repeat**
7: $w^n \leftarrow -\nabla_u F(u^n) = -D_u f\{T[Q_{\mathrm{RF}}(u^n)]\}$ ▷ Compute descent direction
8: **if** $n = 0$ **then** ▷ Initialize step size
9: $s^0 \leftarrow (2|w^0|)^{-1}\mathrm{diam}(D)$
10: **else**
11: $s^n \leftarrow 2|w^{n-1}|(|w^n|)^{-1}s^{n-1}$
12: **end if**
13: $m \leftarrow 0$ ▷ Reset counter
14: $u^{n+1} \leftarrow P(u^n + s^n w^n)$ ▷ Determine step size
15: **while** $F(u^{n+1}) > F(u^n)$ or $u^{n+1} \notin U$ **do**
16: $m \leftarrow m + 1$ ▷ Increase counter
17: **if** $m = m_{\max}$ **then**
18: STOP
19: **end if**
20: $s^n \leftarrow s^n/2$ ▷ Bisect step size
21: $u^{n+1} \leftarrow P(u^n + s^n w^n)$
22: **end while**
23: **until** $|u^{n+1} - u^n| \leq \theta$
24: $\bar{u} \leftarrow u^{n+1}$
25: $l \leftarrow l + 1$ ▷ Proceed to next level
26: **end while**

Here, the derivative $\partial_{p_i}\phi$ of the potential ϕ with respect to the shape parameter p_i is calculated by the following PDE system obtained by a transformation of the potential equation (1) with boundary conditions (2):

$$\int_{D\setminus D_{\mathrm{el}}} \sigma\langle\nabla\partial_{p_i}\phi, \nabla v\rangle dx = 0$$

$$\partial_{p_i}\phi = -\langle\nabla\phi, x_{p_i}\rangle \quad \forall\, x \in \partial D_{\mathrm{el}}.$$

For the integration in the objective function we use a tensor-product trapezoidal rule. The search for the optimal step size is performed with a variant of Armijo's rule (cf., e.g., [42]) (lines 8–22 of Algorithm 1). Note that for each test in the while-condition (see Algorithm 1, line 15), an evaluation of the complete system of PDEs (9), and the objective function are needed. To obtain representations of the vascular structure D_{v} and of the lesion D_{t} on coarse grids we use a bilinear restriction frequently used in multigrid methods [60] with an additional threshold for the tumor and the vessels to obtain sharp boundaries.

For more details of the multiscale gradient descent approach we refer the reader to [10]. There, we have also verified the multiscale optimization process on the basis of an artificial example where the optimal probe placement is qualitatively known.

2.3.3 Sensitivity Analysis

From an appropriate approximation of the stochastic process describing the optimal probe placement (see Section 2.4), we can analyze the sensitivity of the system to perturbations in the material parameters.

An indicator for the robustness (or more precisely the global behavior) of the optimal probe placement with respect to variations in the material parameters is obtained by a direct analysis of the probability density function of the probe placement. For the sensitivity analysis of the optimal probe orientation (which has values on the two-dimensional sphere) we perform a visualization of the PDF by a color coding of the sphere (see Section 3.3). The PDF of the optimal probe position is a mapping $\mathbb{R}^3 \to \mathbb{R}$ which could be visualized through volume rendering. However, a deep understanding and analysis of the respective three-dimensional PDF could be obtained only by an interactive three-dimensional display of the data. Moreover, in general, the PDF is not calculable analytically; one has to evaluate the stochastic process or its approximation at a large number of sampling points to get an appropriate approximation of the PDF. For more details we refer the reader to [61] and in particular to [62].

An analysis of the stochastic moments is more accessible, as it can be obtained more easily from the discrete representation of the stochastic process bypassing the construction of the PDF. Thus, for the sensitivity analysis of the optimal probe position, we consider the covariance matrix of the joint distribution of the probe position's components. For the joint distribution of the coordinates of the optimal probe position $\bar{p}(\xi) = [\bar{p}_x(\xi), \bar{p}_y(\xi), \bar{p}_z(\xi)]$ we have

$$\mathrm{Cov}[\bar{p}] = \big(\mathrm{Cov}[\bar{p}_c, \bar{p}_d]\big)_{c,d\in\{x,y,z\}}, \quad \text{where} \quad \mathrm{Cov}[\bar{p}_c, \bar{p}_d] = \mathbb{E}\big[(\bar{p}_c - \mathbb{E}[\bar{p}_c])(\bar{p}_d - \mathbb{E}[\bar{p}_d])\big] \tag{20}$$

for all pairs of coordinates $c, d \in \{x, y, z\}$. The covariance matrix is a symmetric (in this case 3×3) matrix that quantifies how the coordinates of the optimal probe position are coupled through the random variable ξ. If this matrix were diagonal, the coordinates would be independent. The covariance matrix can be visualized as an ellipsoid, whose principal axes are aligned with the matrix's eigenvectors and whose extension is scaled with the square root of the corresponding eigenvalues. In Section 3 we will use exactly this way of visualizing the sensitivity of the probe position. In fact, this approach can be interpreted as a principal component analysis of the PDF: large ellipsoids imply that the distribution is wide (has a high variance) in the corresponding direction; small ellipsoids indicate narrow distributions; cigar-shaped ellipsoids indicate (approximate) independence of two components; etc.

Remark

We emphasize that special care must be taken concerning the accuracy of the numerical solvers involved. In [63] Kaipio and Somersalo discuss that limited numerical accuracies (i.e., discretization errors) can sometimes (effectively or ineffectively) be interpreted as the behavior of a random process and thus as sensitivity of our problem. Consequently, in our numerical experiments shown in Section 3 we have set the stopping criteria of the iterative solvers as well as for the optimization loops appropriately.

2.4 Discretization

We now discuss our approach for both the spatial discretization of the problem and the stochastic discretization of the problem. For the spatial discretization we will use a composite finite element approach and for the stochastic dimensions an adaptive sparse grid collocation method will be applied. As collocation methods are nonintrusive discretization variants for stochastic problems, we can easily estimate the effort needed for our computations as the number of collocation points times the effort for one deterministic optimization. In the setting described below, the computational effort for one deterministic optimization is about 2 h on a standard contemporary PC. For the sensitivity analyses shown in Section 3 we needed several hundred hours of computational time; however, as the adaptive collocation approach can be parallelized, straightforwardly computed clusters can accelerate the analysis enormously.

2.4.1 Spatial Discretization

For the discretization of the elliptic boundary value problems (9a) and (9b) with boundary conditions (2) and (7) we use a composite finite element (CFE) approach on the three-dimensional uniform Cartesian grids induced by

the underlying medical image data. Composite finite element functions are characterized by an enriched set of basis functions, which take into account particular properties of the solution that are consequences of interfaces or domain boundaries. In fact, the CFE basis functions allow one to resolve kinks of basis functions or supports of basis functions which are not resolved by the computational grid. Thus, CFE can be seen as a kind of adaptivity which is built into the set of shape functions in contrast to the classical grid adaptivity with local mesh refinement.

In the simulation and optimization of RF ablation, discussed here, the main advantage of CFEs over the classical finite element approach is a better resolution of the RF probe's geometry. In fact, with CFEs the geometry of the RF probe is built into the shape of the basis functions, which yields high resolution of the probe even on structured grids, allowing for a combination of the adaptivity and the efficiency of structured hexahedral grids. Furthermore, in our numerical experiments we determined that good resolution of the RF probe has a significant impact on the robustness of the optimization of the RF probe placement, which will be described later. For details on the CFE method we refer the reader to [64–66].

For reasons of analogy we restrict the following description to the problem (9b) which we assume to be adjusted to homogeneous boundary conditions in the usual way. We obtain the weak form by multiplying the corresponding PDE with a test function v. Integration by parts leads to

$$(\lambda \nabla T, \nabla v)_{2,D} + (\nu T, v)_{2,D} = (Q_{\mathrm{RF}} + \nu T_{\mathrm{body}}, v)_{2,D} \tag{21}$$

for all test functions v, where $(\cdot,\cdot)_{2,D}$ denotes the L^2 scalar product over D.

In a second step we discretize this variational problem by restricting (21) to a finite dimensional space V^h consisting of piecewise trilinear, globally continuous shape functions of our finite element space. Note that our CFE basis functions are adapted on the boundary of the RF probe, such that the probe's geometry is approximated sufficiently well on the grid.

Denoting the vector of nodal values t_i of the temperature with $\vec{t} = (t_1, \ldots, t_n)^T$ and the vector of nodal values r_i of the right-hand side with $\vec{r} = (r_1, \ldots, r_n)^T$, we finally have to solve

$$(\mathbf{L}[\lambda] + \mathbf{M}[\nu])\, \vec{t} = \vec{r}\ ,$$

where the *stiffness matrix* $\mathbf{L}[\lambda]$ and the *mass matrix* $\mathbf{M}[\nu]$ are given by

$$L_{ij}[\lambda] = (\lambda \nabla \psi_i, \nabla \psi_j)_{2,D} \quad \text{and} \quad M_{ij}[\nu] = (\nu \psi_i, \psi_j)_{2,D}\ .$$

Since the matrix $(\mathbf{L}[\lambda] + \mathbf{M}[\nu])$ is symmetric and positive definite, this system can be solved by, e.g., a conjugate gradient (CG) method.

2.4.2 Stochastic Discretization

For the sensitivity analysis as discussed in the previous paragraphs, we have to traverse through the stochastic space and evaluate the optimal probe location for various realizations of the uncertain material parameters. Roughly speaking, we are thus analyzing the response surface of the optimal probe location as a function of the uncertain material parameters.

As briefly described in the Introduction, a multitude of approaches has been developed for the discretization of SPDEs. Here, we follow the adaptive sparse grid collocation approach by Ma and Zabaras [13]. This approach combines the sampling character of collocation methods with adaptivity in the stochastic space, thus imposing low regularity assumptions on the underlying stochastic process. Due to the sampling nature we can easily use the optimization algorithm presented above.

A classical and very popular sampling approach is the Monte Carlo (MC) method. Thereby M realizations $\boldsymbol{\xi}_j$, $j = 1, \ldots, M$ of the vector of random variables $\boldsymbol{\xi}$ are generated. Consequently, M deterministic problems are solved, which are obtained from the deterministic optimization problem (19) by considering the realizations of the electric and thermal conductivity σ and λ corresponding to $\boldsymbol{\xi}_j$. Finally, the statistics of the corresponding samples of the optimal probe placement $\bar{u}(\boldsymbol{\xi}_j) = [\bar{p}(\boldsymbol{\xi}_j), \bar{a}(\boldsymbol{\xi}_j)]$ is analyzed to yield the desired sensitivity analysis. The MC approach is

known to be extremely robust and requires no assumptions on the smoothness of the underlying stochastic processes. However, the convergence is very slow and goes asymptotically with $1/\sqrt{M}$.

Other sampling approaches for the solution of SPDEs are based on the construction of interpolating functions. Analogous to classical interpolation and quadrature, such methods are either used to perform the integration over the stochastic space in order to evaluate the stochastic moments of the process under investigation, or they are simply used to construct an approximation of the stochastic process.

It is popular to use a set of quadrature points $\{\boldsymbol{\xi}_j\}_{j=1}^{Q}$ which lie on a sparse grid in the stochastic space (see Fig. 3, left) generated by Smolyak's algorithm [67]. In Smolyak's algorithm a one-dimensional interpolation rule is extended to multiple dimensions with a special tensor-product construction. For the choice of the one-dimensional collocation points there are several other options, among them equidistant points (Newton-Cotes formula), or the extrema of the Chebyshev polynomials (Clenshaw-Curtis formula). For the adaptive collocation approach followed here (cf. [13]), the use of equidistant points is more convenient as it allows for easier local refinement of the stochastic grid (see Fig. 3, right).

In the following we will explain the adaptive sparse grid collocation approach in one dimension. For the ease of the presentation we will treat the actual pair of random variables $[\sigma(\boldsymbol{\xi}), \lambda(\boldsymbol{\xi})]$ used in our application as an element of a one-dimensional stochastic space, accepting the resulting misuse of notation. Let us assume that Smolyak's algorithm yields an interpolant for the optimal probe location $\bar{u}$

$$\tilde{u}^i(\boldsymbol{\xi}) = \sum_{j=1}^{Q_i} \bar{u}(\boldsymbol{\xi}_j^i) h_j^i(\boldsymbol{\xi}) = \sum_{j=1}^{Q_i} \mathcal{S}[\sigma(\boldsymbol{\xi}_j^i), \lambda(\boldsymbol{\xi}_j^i)] h_j^i(\boldsymbol{\xi}) \tag{22}$$

on a set of collocation points $\{\boldsymbol{\xi}_j^i\}_{j=1}^{Q_i}$. Here $h_j^i(\boldsymbol{\xi}_k^i) = \delta_{jk}$ denotes the corresponding set of nodal basis functions and $\mathcal{S}$ denotes the solution operator for the deterministic optimization problem from the previous sections, i.e., $\bar{u}(\boldsymbol{\xi}) = \mathcal{S}[\sigma(\boldsymbol{\xi}_j^i), \lambda(\boldsymbol{\xi}_j^i)]$. The index i refers to the level of refinement of the sparse Smolyak grid, i.e., we have a sequence of interpolations $\tilde{u}^i$, which are constructed with varying numbers Q_i of collocation points $X^i := \{\boldsymbol{\xi}_j^i\}_{j=1}^{Q_i}$, $i \in \mathbb{N}$. Due to the construction of the sparse grids the sets of collocation points are nested, i.e., $X^i \subset X^{i+1}$.

The key to the adaptive sparse grid collocation lies in the analysis of the incremental interpolant

$$\Delta^i(\bar{u}) = \tilde{u}^i - \tilde{u}^{i-1}.$$

Using the nestedness of the collocation points and (22) we arrive at

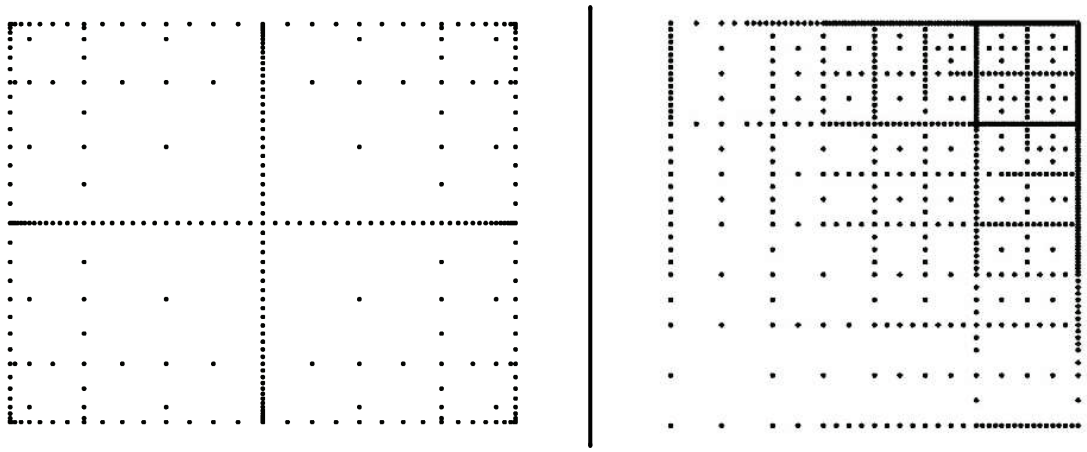

FIG. 3: Two-dimensional sketch of a distribution of grid nodes obtained with Smolyak's algorithm (left) and of a uniform, adaptive distribution of nodes for the two-dimensional stochastic interpolation with piecewise multilinear, hierarchical ansatz functions (right).

$$\Delta^i(\bar{u}) = \sum_{\boldsymbol{\xi}_j^i \in X^i \setminus X^{i-1}} \left(\mathcal{S}[\sigma(\boldsymbol{\xi}_j^i), \lambda(\boldsymbol{\xi}_j^i)] - \tilde{u}^{i-1}(\boldsymbol{\xi}_j^i) \right) h_j^i =: \sum_{\boldsymbol{\xi}_j^i \in X^i \setminus X^{i-1}} \omega_j^i \, h_j^i, \tag{23}$$

where $\omega_j^i := \mathcal{S}[\sigma(\boldsymbol{\xi}_j^i), \lambda(\boldsymbol{\xi}_j^i)] - \tilde{u}^{i-1}(\boldsymbol{\xi}_j^i)$ is the hierarchical surplus. Starting with $\tilde{u}^0 = 0$, we can construct the interpolant $\tilde{u}^i$ at level i from the interpolant at level $i-1$ using the hierarchical surpluses and the associated basis functions. Due to the enumeration of the collocation points in the sum of (23) the basis functions will be visited in a hierarchical way (cf. Fig. 4) and we arrive at a hierarchical representation of the interpolant in the form

$$\tilde{u}^i(\boldsymbol{\xi}) = \sum_{k \le i} \sum_{\boldsymbol{\xi}_j^k \in X^k \setminus X^{k-1}} \omega_j^k \, h_j^k(\boldsymbol{\xi}). \tag{24}$$

With this representation we can straightforwardly evaluate the moments needed for the sensitivity analysis as discussed in Section 2.3.3. For the expectation we get

$$\mathbb{E}[\tilde{u}^i] = \sum_{k \le i} \sum_{\boldsymbol{\xi}_j^k \in X^k \setminus X^{k-1}} \omega_j^k \int_\Omega h_j^k(\boldsymbol{\xi}) \, d\mu, \tag{25}$$

where the integrals of the basis functions h_j^k can be computed in advance, such that the evaluation of the expectation can be accelerated toward a simple weighted sum of the hierarchical surpluses. To obtain higher order moments or the covariance from (20) we first need to express the product [i.e. $(\tilde{u}^i - \mathbb{E}[\tilde{u}^i])^2$], respectively, $(\bar{p}_c - \mathbb{E}[\bar{p}_c])(\bar{p}_d - \mathbb{E}[\bar{p}_d])$] in the hierarchical representation (24) and then evaluate its expectation with (25).

In the case of interpolation in a multidimensional stochastic space, hierarchical difference spaces must be constructed, which lead to the analog definition of the hierarchical surpluses. We refer the reader to [13] for details on the multidimensional adaptive sparse grid collocation approach. In Fig. 3 (right) we show an adaptive hierarchical sparse grid resulting from the construction described above.

For the construction of an adaptive sparse grid, the hierarchical surpluses are used as indicators for the smoothness of the interpolation. Given a threshold ε, hierarchical basis functions h_j^i are refined (i.e., the corresponding collocation points in the sparse Smolyak grid are added) if the corresponding hierarchical surplus ω_j^i fulfills $\|\omega_j^i\| \ge \varepsilon$. According to [13] the hierarchical surpluses tend to zero with increasing level i if the process u is smooth. At discontinuities the magnitude of the hierarchical surpluses will not decrease but roughly speaking indicate the size of the jump.

Note that in the application of the adaptive sparse grid collocation method to the optimal probe placement problem we are working with two different thresholds, θ and ε. As described above, θ is the criterion steering the stopping of the optimization algorithm, thus it can be interpreted as an accuracy associated with the optimal probe locations obtained by the algorithm. We also have the smoothness indicator ε, which steers the refinement of the adaptive stochastic grid. We emphasize that these criteria cannot be chosen independently, but we need to respect a compatibility condition. In fact, as the stopping criterion θ can be seen as an indicator of uncertainty or error for the values of u at the collocation points $\boldsymbol{\xi}_j^i$, we need $\varepsilon > 2\theta$ in order to avoid meaningless refinement of the adaptive stochastic grid.

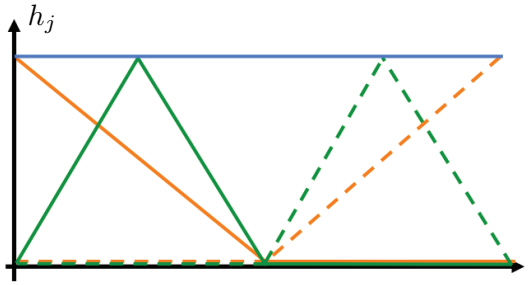

FIG. 4: A set of piecewise multilinear, hierarchical ansatz functions in one dimension is shown.

3. RESULTS

In the following we will evaluate the concepts presented in the preceding sections on the basis of a real RF ablation case. From CT data, which have been segmented with the methodology from [50], we obtain the geometrical description of the computational domain. This includes the representation of the tumor as well as the vascular system in the vicinity of the tumor. The tumor has main axes of approximate length 45.9, 41.9, and 36.2 mm. We place it into a computational domain D of extent $60 \times 60 \times 60\,\mathrm{mm}^3$, which is discretized with a fine grid of 64^3 cells. For the multiscale optimization we consider one coarser grid having 32^3 cells. Our grid width is thus $h = 60/64\,\mathrm{mm} = 0.9375\,\mathrm{mm}$.

We consider the material parameters to be uniformly distributed based upon values found in the literature [3, 4, 6]. In our computations the thermal conductivity $\lambda = (\lambda_\mathrm{n}, \lambda_\mathrm{t}, \lambda_\mathrm{v})$ is distributed uniformly in [0.47,0.64] $\times$ [0.51,0.77] $\times$ [0.51,0.54] $[\mathrm{W/Km}]$ and the electric conductivity $\sigma = (\sigma_\mathrm{n}, \sigma_\mathrm{t}, \sigma_\mathrm{v})$ is distributed uniformly in [0.17, 0.60] $\times$ [0.64, 0.96] $\times$ [0.67, 0.86] $[\mathrm{S/m}]$. For the perfusion term (8) we take $\varkappa_{\text{cap}} = 0.006067\,\mathrm{s}^{-1}$ and $\varkappa_{\text{vessel}} = 0.05\,\mathrm{s}^{-1}$. The value for the blood density is $\rho_{\text{blood}} = 1059.0\,\mathrm{kg/m}^3$, and the heat capacity of blood is set to $c_{\text{blood}} = 3850.0\,\mathrm{J/kgK}$ (cf. Section 2 and [3, 6]). In our study, all these latter values are taken to be deterministic, although they are clearly associated with measurement errors and uncertainty as well.

A monopolar probe with radius $1.2\,\mathrm{mm}$ and with an electrode length of $20\,\mathrm{mm}$ is applied. The electric generator has an inner resistance of $80\,\Omega$, and it is set up to a power of $30\,\mathrm{W}$.

For the ASGC discretization of the vector-valued position and orientation of the probe positioning, we need two stopping criteria for the placement $\bar{p}$, as well as for the direction $\bar{a}$. In our computations we set $\varepsilon_p = 1\,\mathrm{mm}$ and $\varepsilon_a = 5^\circ$, which means that the refinement continues until the hierarchical surpluses of position and orientation are less than $1\,\mathrm{mm}$ and 5°.

As settings for the deterministic optimization, which is performed at each collocation point, we use $\alpha = 0.5$ to regularize the objective function f in (18). The stopping criteria in the optimizer are set to $\theta_p = 10^{-6}\,h = 9.375 \times 10^{-7}\,\mathrm{mm}$ and $\theta_a = 0.057^\circ$ for the probe location and the probe orientation, respectively. For the iterative solvers used in the computation of the forward problem, i.e., the deterministic PDE, we use an accuracy of machine zero 10^{-15} for the decrease of the residual. For the optimization, the initial probe position is always located at a distance of $11.25\,\mathrm{mm}$ in each coordinate direction from the center of D. The initial orientation is $a = (5, 2, 3)$, projected on the sphere (i.e., normalized to length 1). With these settings the optimization of the probe location for one sampling point in the stochastic space typically takes about $2\,\mathrm{h}$ on a standard desktop PC with an Intel® Core 2 Duo™ $2.93\,\mathrm{GHz}$ processor and $4\,\mathrm{GB}$ RAM. For the computations shown here we have used parallelized code on 48 processors. Thereby the collocation samples have been computed by different nodes running the original deterministic code with the respective material parameter values. The collection of the individual results and the computation of the hierarchical surpluses has been managed by a master process.

Remark
To guarantee that the size of our computational domain does not influence the result of the optimizer, we have performed a comparison between forward simulations using Dirichlet or Neumann boundary conditions at ∂D. Both temperature profiles differ at most by $0.45\,\mathrm{K}$ [Kelvin] in the interior of D, i.e., at locations which are more than $10\,\mathrm{mm}$ apart from ∂D. Closer to the boundary, i.e., for locations which lie in a ring with radius $10\,\mathrm{mm}$ around ∂D, the temperatures differ more. In particular, the largest deviation of $4.93\,\mathrm{K}$ appears at the outer boundary ∂D. We conclude that in the vicinity of the lesion the particular choice of boundary condition does not influence the result significantly.

3.1 Sensitivity of the Temperature

To start with the sensitivity analysis we investigate the influence of the uncertain material parameters on temperature, which is determined by the forward model (see Section 2.1). Here we do not take the ASGC discretization into account but perform a simple uniform sampling of the six-dimensional stochastic space for stochastic σ and λ by $3^6 = 729$ grid points, such that all 3^6 combinations of σ and λ at the interval boundaries and at the middle of the intervals are considered. We then determine the values of σ and λ for which the L^∞-norm (maximum values) of the temperatures differs most.

We find that we get the largest difference between the temperatures for the parameters $(\sigma_n, \sigma_t, \sigma_v, \lambda_n, \lambda_t, \lambda_v) = (0.17, 0.64, 0.67, 0.64, 0.51, 0.54)$ and $(\sigma_n, \sigma_t, \sigma_v, \lambda_n, \lambda_t, \lambda_v) = (0.60, 0.64, 0.86, 0.47, 0.77, 0.51)$. In Fig. 5 we show the $50°C$ isosurface of those temperature realizations (left and middle) as well as the $30\,K$ [Kelvin] isosurface of the difference of these temperature profiles (right).

The results match our intuition, since for a large value of the thermal conductivity λ_t within the tumor region (Fig. 5, middle) the high temperature around the probe diffuses faster away than for a small value of λ_t. From the results we see a significant difference in the shape of the $50°C$ temperature profiles, in particular close by the vessels (see left and middle image of Fig. 5). Moreover, we see that the largest temperature difference appears around the end of the probe's electrode which lies close by the vascular system (see right image of Fig. 5). Further, we notice that obviously there exist material parameter settings for which a complete ablation of the tumor is not achieved (Fig. 5, middle). This further motivates the consideration of the material parameter uncertainty for the planning of RF ablation.

3.2 Sensitivity of the Optimal Probe Location

In the following three subsections we will focus on the actual sensitivity analysis of the optimal probe location and optimal probe orientation. If we consider the full complexity of the underlying material parameter uncertainty, we have to analyze and visualize a six-dimensional stochastic space (three dimensions each for σ and λ), which is mapped to the five-dimensional space U of admissible probe placements. Thus the visualization and analysis of PDFs of the probe placement is not straightforward, as they are mappings $\mathbb{R}^5 \supset U \to \mathbb{R}$.

Moreover, we need to be aware that in the optimization we are dealing with a very complex nonconvex energy landscape, which is characterized by local optima and possibly nonexisting and nonunique global optima (see also the discussion in Section 2.3). In our numerical experiments, we found that the optimization of the probe's position only (keeping its orientation fixed), and the optimization of the probe's orientation only (keeping its position fixed) have fewer local optima than the optimization of both quantities at the same time. Thus, in the following we first analyze the sensitivity of the optimal probe position and orientation separately (i.e., independent of each other) (see Figs. 6 and 7) and in a further step then consider the sensitivity of the combined optimization of both quantities (see Figs. 8 and 9).

So let us first keep the probe's orientation fixed at the starting value and just optimize for the location. From the hierarchical representation (24) we compute the first moment and the covariance matrix using (25) and (20). As described in Section 2.3.3 we compute its eigenvalues and eigenvectors yielding an ellipsoidal representation. In the

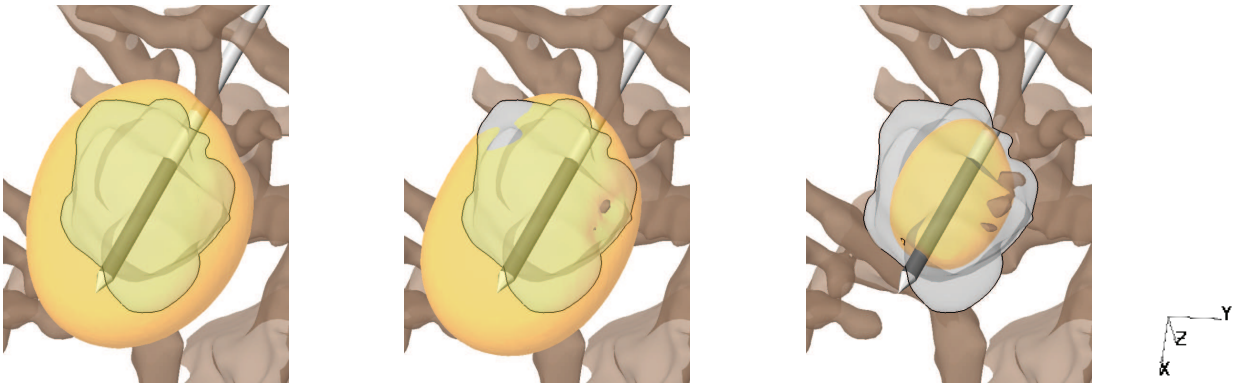

FIG. 5: Left and middle: We show the $50°C$ isosurface of two different temperatures obtained for different realizations of σ and λ. Right: Visualization of the $30\,K$ isosurface of the difference of the two temperatures, whose $50°C$ isosurfaces are presented on the left. In all images the vascular system D_v is displayed in beige-brown and the tumor lesion D_t is displayed in a transparent gray color. Moreover, all isosurfaces of temperatures are displayed in transparent yellow. Hence, the superposition of the gray tumor and the yellow isosurface of the temperature appears in a greenish color.

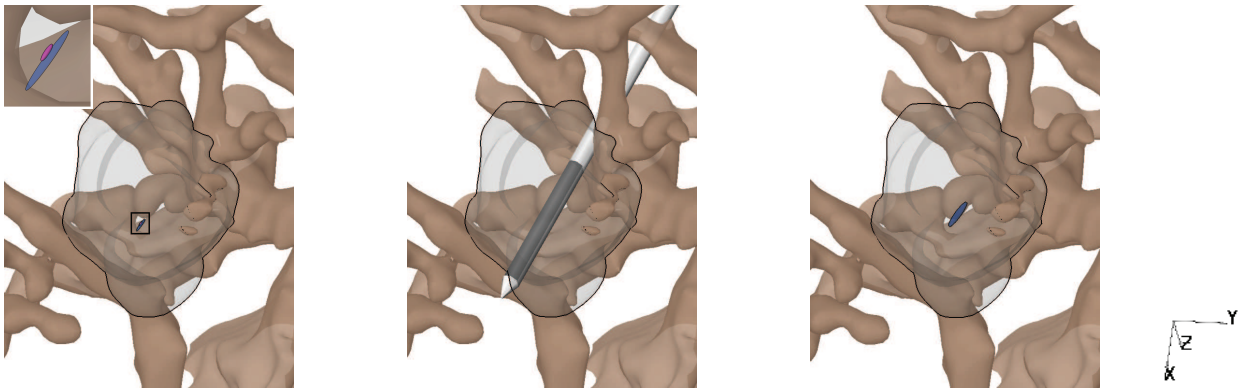

FIG. 6: Visualization of the sensitivity of the optimal probe position through an ellipsoidal representation of the covariance matrix. The sensitivity with respect to variations in the electric conductivity σ (left, blue ellipsoid) and thermal conductivity λ (left, pink ellipsoid) are shown. In addition, we show the RF probe drawn at the mean of the corresponding placement's distribution for stochastic σ and λ, respectively (middle). Moreover, the sensitivity with respect to a larger variation of σ (i.e., $\sigma \in [0.1, 3.0]^3$ $[\mathrm{S/m}]$) is visualized (right). As before, the vascular system D_v is displayed in beige-brown and the tumor lesion D_t is displayed in a transparent gray color.

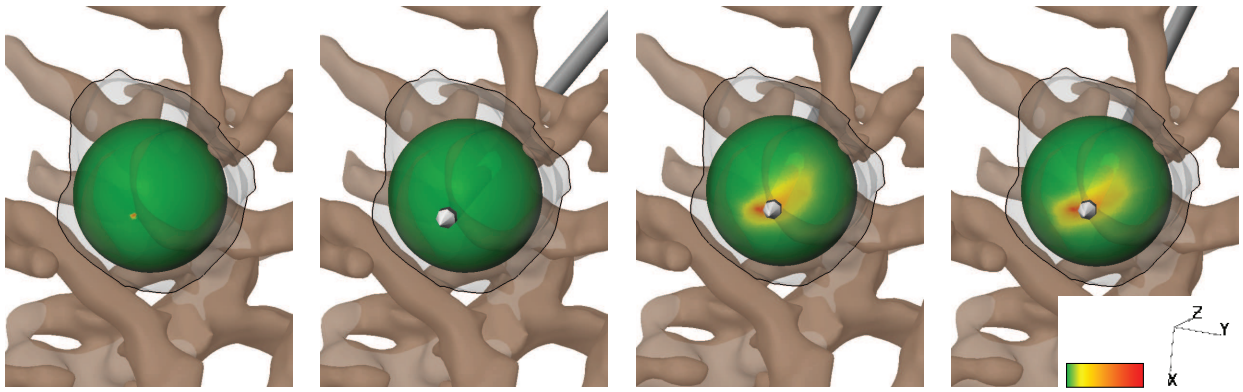

FIG. 7: Visualization of the sensitivity (i.e., the PDF) of the optimal probe orientation through a color coding of the sphere. As shown by the color ramp on the right, green colors indicate unlikely orientations, whereas red colors show likely orientations. On the left we see the sensitivity with respect to variations in σ within the rather small ranges presented at the beginning of Section 3. In the left middle image we additionally draw the RF probe at the mean of the placement's distribution. On the right images we see the sensitivity with respect to larger variations of σ (i.e., $\sigma \in [0.1, 3.0]^3$ $[\mathrm{S/m}]$) for level 10 (middle, right) and for the previous refinement level 9 (right) again with the RF probe drawn at the mean of the placement's distribution. As in the previous figures, the vessels D_v are displayed in beige-brown and the tumor D_t is displayed in transparent gray.

visualization shown here we draw the ellipsoid centered at the expected probe location; the principal axes are aligned with the eigenvectors; and the radii are scaled with the square root of the eigenvalues.

In Fig. 6 we embed the ellipsoid in the surrounding anatomy of the CT data set of a real RF ablation case. We visualize the sensitivity of the probe position (with fixed orientation) with respect to variations in σ (left, blue ellipsoid) and λ (left, pink ellipsoid). The RF probe is drawn at the expectation of the corresponding placement's distribution for stochastic σ and λ, respectively (middle).

We see that our model (i.e., our optimal probe position) shows no significant sensitivity with respect to variations in σ or λ, since the corresponding ellipsoids are very small (see Fig. 6, left). Moreover the expectation of the placement

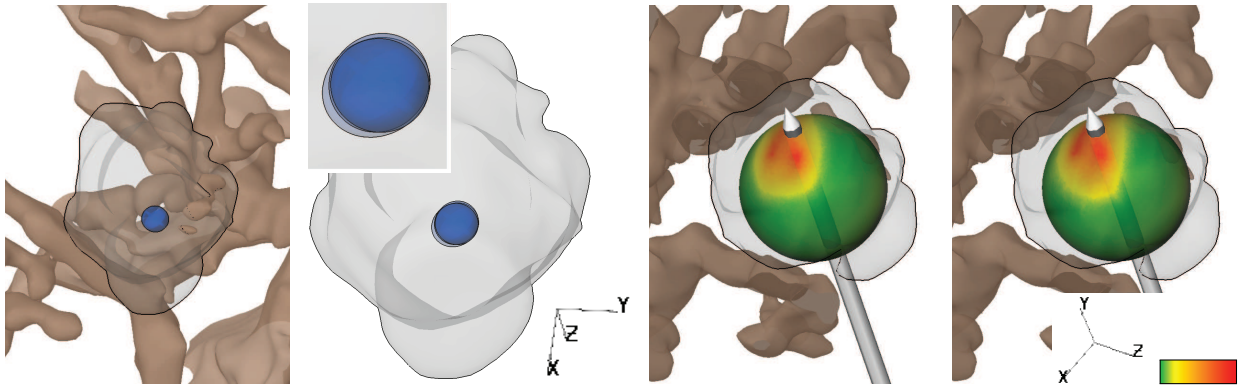

FIG. 8: Visualization of the sensitivity of the optimal probe position (left, representation of the covariance matrix via blue ellipsoid) and orientation (middle right, coloring of the sphere) with respect to variations of σ in the ranges described at the beginning of Section 3 and obtained for the combined optimization of the probe's position and orientation up to level 9. In the left middle image we see the corresponding sensitivity results for the optimal probe position and for the last three refinement levels (level 7, 8, and 9) of the stochastic grid. In the right image we see the sensitivity result for the optimal probe orientation and for the previous refinement level (level 8). Again as in the previous images, the segmented vascular system D_{v} (if shown) is displayed in beige-brown and the segmented lesion D_{t} is displayed in transparent gray.

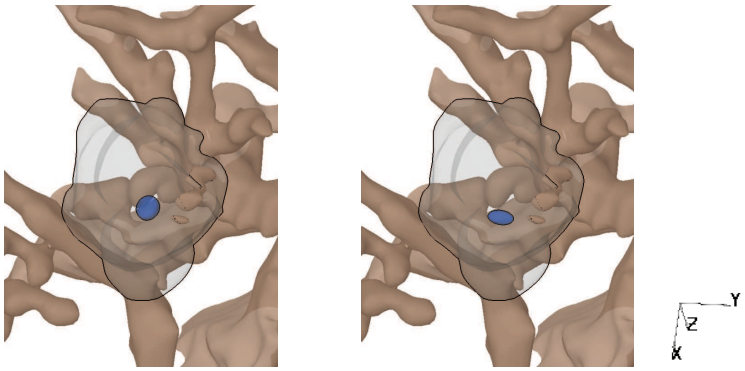

FIG. 9: Visualization of the sensitivity of the optimal probe position (right) for the combined optimization of position and orientation and with respect to variations in σ and λ at stochastic refinement level 6. On the left we show the corresponding result for the combined optimization with only variations in σ, again at refinement level 6.

for stochastic σ differs from the expectation for stochastic λ by only $0.2\,\mathrm{mm}$ (see Fig. 6, middle). Also, for simultaneous variations in σ and λ we did not obtain a significant sensitivity in our numerical experiments. Consequently the results are not shown here.

In a second step of this numerical experiment we assume that the ranges for our material parameters are further accompanied by measurement errors and carry additional uncertainty because they are taken from animals or cadaveric tissue. Thus, we consider $\sigma = (\sigma_{\mathrm{n}}, \sigma_{\mathrm{t}}, \sigma_{\mathrm{v}}) \in [0.1, 3.0]^3\ [\mathrm{S/m}]$. From these calculations we see a slightly larger sensitivity of the optimal probe position (see Fig. 6, right).

In summary, our results show that the sensitivity of the optimal probe position with respect to uncertainties in the electric and/or thermal conductivity is small when analyzing an optimization of only the probe position with fixed orientation. However, the sensitivity of the optimal probe position with respect to tissue parameters increases for a combined optimization of position and orientation (see Section 3.4). Moreover, we have to keep in mind that results may change for different patient data, the analysis of which is an important future task.

3.3 Sensitivity of the Optimal Probe Orientation

In the second numerical experiment, we consider the sensitivity of the optimal probe orientation $\bar{a}$, keeping the probe's position fixed. As we are again expecting the greater sensitivity with respect to the electric conductivity here, we investigate variations in σ only. We are now dealing with a stochastic process, which has values on the two-dimensional sphere S^2 (as we identify orientations with unit vectors). On the sphere we can easily visualize a PDF, e.g., by a color coding as shown in Fig. 7. In this figure we see the resulting PDF of the optimal probe orientation $\bar{a}$ for σ varying within the ranges presented at the beginning of Section 3 (Fig. 7, left and middle left) as well as for the extended range $\sigma \in [0.1, 3.0]^3$ $[\mathrm{S/m}]$ (Fig.7, middle right [level 10] and right [previous level 9 for comparison]).

In the computation with the extended range of σ we found that until a refinement level of $i = 10$ the hierarchical surpluses had not fallen below the prescribed threshold of $\varepsilon_a = 5^\circ$. According to [13] the hierarchical surpluses would decrease to zero, i.e., the refinement would stop, if the process were smooth. So, our observation could be an indication of a discontinuous or possibly oscillatory response surface or an even more delicate interplay between the various parameters of our algorithms and the stopping criteria involved. In fact, more detailed and thorough mathematical and numerical analysis would be needed, which is not further discussed here. However, from the viewpoint of the practical problem of providing important information to the attending radiologist, we note that the accuracy achieved is sufficient. We refer to the next section in which we will discuss this aspect in more detail. The results shown here used about 480 h of wall time for the parallel code.

The results shown in Fig. 7 confirm our observation from the analysis of the optimal probe location: We have a weak dependence on σ for variations within the rather small ranges presented at the beginning of Section 3 and a more significant dependence on σ for large variations of this three-dimensional tissue parameter.

Again, we analyzed the sensitivity of the optimal probe orientation with fixed position with respect to variations in the thermal conductivity λ within the rather small ranges presented at the beginning of Section 3. As before, the results do not differ much from the corresponding results for a stochastic electric conductivity σ (i.e., they reveal no significant sensitivity), thus we do not show them here.

3.4 Sensitivity of Joint Optimization of Position and Orientation

Our final experiments consider the sensitivity analysis of the simultaneous optimization of the probe's position and orientation with respect to variations in the electric conductivity σ only (see Fig. 8 and Fig. 9, left) and with respect to variations in both the electric and thermal conductivity σ and λ (see Fig. 9, right).

For the first experiment (only σ uncertain), the electric conductivity varies within the ranges presented at the beginning of Section 3. The results are reported in Fig. 8, where we see a much larger sensitivity of the optimal probe position than for the separate optimization of only the probe's position from Fig. 6.

Again we found that up to refinement level $i = 9$ (and up to a wall time of about 520 h for the parallel code) the hierarchical surpluses did not decrease below the prescribed thresholds $\varepsilon_p = 1\,\mathrm{mm}$ and $\varepsilon_a = 5^\circ$. In the figure we visualize the corresponding ellipsoid for the last three refinement levels 7, 8, and 9 (Fig. 8, middle left). On the right images of Fig. 8 we show the sensitivity of the optimal probe orientation, which we obtained for this combined optimization for refinement levels 9 (middle right) and 8 (right).

As described in Section 2.3.3 we can analyze the covariance matrix by evaluating its eigenvalues β_j, $j = 1, 2, 3$, which are reported in Table 1 for the case considered here. We also see from the eigenvalues that the refinement has not stopped and thus the eigenvalues have not converged with increasing refinement level i. As stated in the previous subsection a more detailed mathematical and numerical analysis would be needed to understand the results we see here.

However, the pictures shown in Figs. 7 and 8 show almost no visual difference between the last refinement levels. In fact, if we would use these pictures to communicate the result of the analysis to the attending radiologist, he/she would not be able to see a significant difference, respectively, make different decisions, based on either image. Furthermore, taking into account that our computations are based on units of millimeters, the eigenvalues shown in Table 1 have sufficient accuracy: A radiologist will not be able to place a probe, which has a diameter of 1 mm, with an accuracy of fractions of millimeters.

TABLE 1: Eigenvalues β_j, $j = 1, 2, 3$ of the covariance matrix and number of used collocation points for the sensitivity analysis of the combined optimization of the probe's position and orientation with respect to uncertain electric conductivity σ (see also Fig. 8) for the stated refinement levels.

Refinement Level i	Number of colloc. pts.	β_1	β_2	β_3
4	162	3.25665	1.55417	1.33213
5	392	5.39707	2.6754	1.45017
6	942	4.89901	2.85342	1.6954
7	2156	5.90408	3.74795	2.13096
8	4412	5.91824	3.30217	2.23831
9	8470	5.5201	2.84418	2.53418

Finally, we evaluate the sensitivity of the combined optimization of position and orientation for uncertainty in both σ and λ. This is the most complex configuration treated with the approach discussed in this work: We are now analyzing the sensitivity of the mapping from $\mathbb{R}^6 \ni (\sigma, \lambda)$ to $\mathbb{R}^5 \ni \bar{u} = (\bar{p}, \bar{a})$. The collocation in the six-dimensional stochastic space is of enormous numerical complexity. The results shown here used about 720 h of wall time.

In Fig. 9 (right) we show the sensitivity of the optimal probe position for this combined optimization and for σ and λ varying within the ranges presented at the beginning of Section 3. Also for this last experiment, we found that up to refinement level $i = 6$ the hierarchical surpluses did not decrease below the prescribed thresholds for ε_p and ε_a. On the left of Fig. 9 we display the resulting ellispoid for the previous experiment (combined optimization with only σ uncertain) at refinement level 6 to allow for a comparison with the result on the right of Fig. 9 (combined optimization with both σ and λ uncertain) which is obtained for the same refinement level.

We finally conclude that for the combined optimization of the probe's position and orientation and/or for large variations in the electric and/or thermal conductivity the uncertainty of the tissue properties can have a significant influence on the optimal probe placement for RF ablation. However, this sensitivity seems dominantly to be influenced by the electric conductivity σ rather than by the thermal conductivity λ.

4. DISCUSSION AND CONCLUSIONS

We have discussed a model for the optimization of the placement of a monopolar probe in radiofrequency ablation that depends on the electric and thermal conductivity of native liver tissue, tumor tissue, and vessels. The deterministic forward model for the simulation of the temperature distribution of the RF ablation, which is used within our optimization, has been extended to a stochastic PDE model with stochastically distributed material parameters, taking into account the uncertainty associated with electric and thermal conductivities of the tissue. Together with an adaptive sparse grid collocation method, we have evaluated the sensitivity of the optimization results with respect to variations in the material parameters.

We have presented numerical results which are based on a segmented lesion and vascular structures from a real CT scan. Because vector-valued data are optimized (probe location and/or probe orientation) a visualization of the resulting distributions is not straightforward. For the visualization of the distribution of the optimal probe location we presented different approaches. Since a three-dimensional volume rendering of the histograms is difficult to interpret, we use an ellipsoidal representation, which easily reveals the mean and the covariance of the distribution. A visualization of the distribution of the optimal probe orientation is much simpler. Here we showed a color coding of the sphere according to the corresponding PDF.

Our numerical experiments show a significant sensitivity of the temperature profiles resulting from the forward problem with respect to variations in the tissue properties. For the optimization, however, the separate consideration of only the probe position or only the probe orientation does not show any significant sensitivity for realistic variations

in the electric conductivity σ and/or the thermal conductivity λ which are given in the literature for cadaveric animal tissue. If we enlarge the variations in order to account for measurement errors and differences between animal and human tissue we see a slightly more significant sensitivity especially for the optimization of only the probe orientation. If we analyze the combined optimization of the probe's position and orientation, we obtain significant sensitivities, also for the smaller variations of σ.

The optimization of the placement of one monopolar probe presented in this work easily generalizes to an optimization of the placement of a cluster of probes. Also, the study of treatment by bipolar probes, multipolar probes, or umbrella-type probes is possible with the framework presented herein. Our investigations in these fields are still in progress. In addition, the approach presented in this paper can be used for many other models in medical simulation including cryosurgery or irreversible electroporation as well.

With our investigations we have performed a step toward patient-specific modeling in the field of medical simulation—here applied to the optimization of RF ablation. We do not tackle the problem of patient-specific parameters by trying to obtain more accurate material parameters. Instead we consider uncertainty to be an intrinsic attribute of the modeling process. The numerical experiments considered here demonstrate that our approach allows one to quantify the robustness of predictions and optimal probe placements with respect to the uncertainty involved in the model parameters. In this sense our investigations can sensitize the practitioner to problematic cases in which further steps need to be taken to be confident of therapy success. However, the sensitivity analyses are obtained at an extremely high computational cost resulting from the highly complex optimization problem and the enormous number of collocation points that needed to be taken into account.

The acceleration of the sensitivity analysis is an important aspect of our future investigations. This will involve further model reductions and possible simplifications which allow one to more easily traverse the response surface and thus analyze its shape.

In some numerical experiments discussed in this paper, we have not been able to fulfill the stopping criteria of the adaptive refinement in the stochastic space. We will further analyze this effect and expect to gain more insight and understanding of the complex interplay between algorithm and parameters of this extremely complex real world stochastic PDE constrained optimization problem. In the course of these investigations we will study further the sensitivity of the combined optimization of probe position and orientation with respect to uncertainty in several different tissue properties (e.g., electric and thermal conductivity) at the same time.

Further future research directions deal with the optimization of the RF ablation under a refined and time-dependent model for the simulation. Thus, we can take into account the nonlinear dependence of the material parameters on the state of the system as well. Also, the consideration of the perfusion coefficients as sources of uncertainty will be a further direction of research. Figure 10 shows an outlook in this direction. Here, we see the $50^\circ\mathrm{C}$ isosurface of the resulting temperatures of our forward simulation calculated for different values of the relative perfusion rate ν_{vessel}

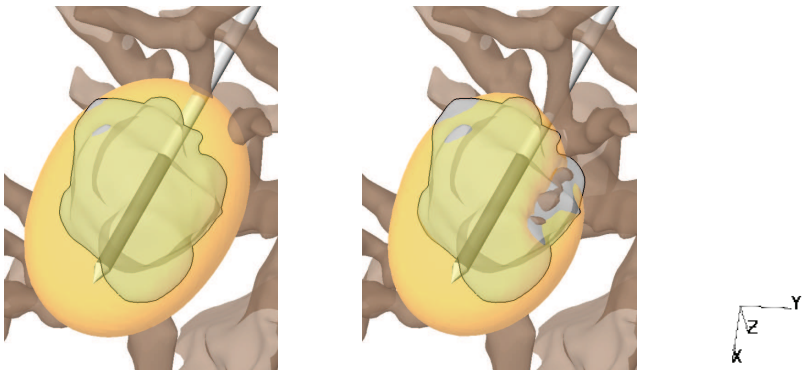

FIG. 10: $50^\circ\mathrm{C}$ isosurface of the temperatures calculated with our forward simulation for $\nu_{\text{vessel}} = 0.006067\,\mathrm{s}^{-1}$ (left) and $\nu_{\text{vessel}} = 0.5\,\mathrm{s}^{-1}$ (right). In both calculations the values of σ and λ have been set to the mean values of the intervals presented at the beginning of Section 3.

(see Section 2.1), i.e., for $\nu_{\text{vessel}} = 0.006067\,\text{s}^{-1}$ (capillary perfusion) and for $\nu_{\text{vessel}} = 0.5\,\text{s}^{-1}$ (strong perfusion for which the temperature within the vascular system approximately remains body temperature). All other tissue parameters (i.e., the conductivity values) have been set to the mean values of the intervals presented at the beginning of Section 3. We see that we get a significant difference in the shape of the corresponding temperature profiles, which motivates a deeper analysis of uncertain perfusion coefficients.

ACKNOWLEDGMENT

The authors would like to thank Professor Dongbin Xiu (Purdue University) and Professor Wolfgang Ring (Graz University, Austria) for beneficial discussions on the topics within this paper. This is a collaborative research project supported under NSF IIS-0914564 (Kirby) coupled NSF IIS-0914447 (Xiu) and through DOE NET DE-EE0004449 (Johnson/Kirby). Infrastructure support provided through NSF-IIS-0751152. This project has been supported by funding from the German Research Foundation DFG under grant no. PE 199/18-1.

REFERENCES

1. Baegert, C., Villard, C., Schreck, P., Soler, L., and Gangi, A., Trajectory optimization for the planning of percutaneous radiofrequency ablation of hepatic tumors, *Comput. Aided Surg.*, 12(2):82–90, 2007.
2. Kim, Y. S., Rhim, H., Cho, O. K., Koh, B. H., and Kim, Y., Intrahepatic recurrence after percutaneous radiofrequency ablation of hepatocellular carcinoma: Analysis of the pattern and risk factors, *Eur. J. Radiol.*, 59(3):432–441, 2006.
3. Stein, T., *Untersuchungen zur Dosimetrie der hochfrequenzstrominduzierten interstitiellen Thermotherapie in bipolarer Technik*, Vol. 22 of Fortschritte in der Lasermedizin, Müller and Berlien, Ecomed, Landsberg, Germany 2000.
4. Deuflhard, P., Weiser, M., and Seebaß, M., A new nonlinear elliptic multilevel FEM applied to regional hyperthermia, *Comput. Vis. Sci.*, 3(3):115–120, 2000.
5. Jain, M. K. and Wolf, P. D., A three-dimensional finite element model of radiofrequency ablation with blood flow and its experimental validation, *Ann. Biomed. Eng.*, 28(9):1075–84, 2000.
6. Tungjitkusolmun, S., Staelin, S. T., Haemmerich, D., Tsai, J.-Z., Cao, H., Webster, J. G., Lee, F. T., Mahvi, D. M., and Vorperian, V. R., Three-dimensional finite-element analyses for radio-frequency hepatic tumor ablation, *IEEE Trans. Biomed. Eng.*, 49(1):3–9, 2002.
7. Kröger, T., Altrogge, I., Preusser, T., Pereira, P. L., Schmidt, D., Weihusen, A., and Peitgen, H.-O., Numerical simulation of radio frequency ablation with state dependent material parameters in three space dimensions, *Lect. Notes Comput. Sci.*, 4191:380–388, 2006.
8. Harth, O., Wasserhaushalt, Stoff und Flüssigkeitstransport, In: Schmidt, R. F. and Thews, G., eds., *Physiologie des Menschen*, Springer, Berlin, 1993.
9. Bowman, H. F., Heat transfer and thermal dosimetry, *J. Microwave Power*, 16(2):121–133, 1981.
10. Altrogge, I., Preusser, T., Kröger, T., Büskens, C., Pereira, P. L., Schmidt, D., and Peitgen, H.-O., Multi-scale optimization of the probe placement for radio-frequency ablation, *Acad. Radiol.*, 14(11):1310–1324, 2007.
11. Haase, S., Ring, W., Altrogge, I., Kröger, T., and Preusser, T., Optimization of probe placement for radio-frequency ablation using shape derivatives, *in preparation*, 2012.
12. Ghanem, R. G. and Spanos, P., *Stochastic Finite Elements: A Spectral Approach*, Springer-Verlag, New York, 1991.
13. Ma, X. and Zabaras, N., An adaptive hierarchical sparse grid collocation algorithm for the solution of stochastic differential equations, *J. Comput. Phys.*, 228:3084–3113, 2009.
14. Xiu, D., *Numerical Methods for Stochastic Computations*, Princeton University Press, Princeton, NJ, 2010.
15. Nobile, F., Tempone, R., and Webster, C. G., A sparse grid stochastic collocation method for partial differential equations with random input data, *SIAM J. Numer. Anal.*, 46(5):2309–2345, 2008.
16. Xiu, D. and Hesthaven, J. S., High-order collocation methods for differential equations with random inputs, *SIAM J. Sci. Comput.*, 27(3):1118–1139, 2005.

17. Welp, C., Siebers, S., Ermert, H., and Werner, J., Investigation of the influence of blood flow rate on large vessel cooling in hepatic radiofrequency ablation, *Biomed. Technol.*, 51:337–346, 2006.
18. Roggan, A., *Dosimetrie thermischer Laseranwendungen in der Medizin*, Vol. 16 of Fortschritte in der Lasermedizin, Müller and Berlien, Ecomed, Landsberg, Germany, 1997.
19. Preusser, T., Weihusen, A., and Peitgen, H.-O., On the modelling of perfusion in the simulation of RF-ablation, *Proc. SimVis*, Magdeburg, 2005.
20. Villard, C., Soler, L., and Gangi, A., Radiofrequency ablation of hepatic tumors: Simulation, planning, and contribution of virtual reality and haptics, *Comp. Meth. Biomech. Biomed. Eng.*, 8(4):215–227, 2005.
21. Butz, T., Warfield, S. K., Tuncali, K., Silverman, S. G., Sonnenberg, E.v., Jolesz, F. A., and Kikinis, R., Pre- and intra-operative planning and simulation of percutaneous tumor ablation, *Lect. Notes Comput. Sci.*, 1935:395–416, 2000.
22. Khalil-Bustany, I. S., Diederich, C. J., Polak, E., and Kirjner-Neto, C., Minmax optimization-based inverse treatment planning for interstitial thermal therapy, *Int. J. Hyperthermia*, 14(4):347–366, 1998.
23. Seitel, A., Engel, M., Sommer, C. M., Radeleff, B. A., Essert-Villard, C., Baegert, C., Fangerau, M., Fritzsche, K. H., Yung, K., Meinzer, H. P., and Maier-Hein, L., Computer-assisted trajectory planning for percutaneous needle insertions, *Med. Phys.*, 38(6):3246–3259, 2011.
24. Villard, C., Baegert, C., Schreck, P., Soler, L., and Gangi, A., Optimal trajectories computation within regions of interest for hepatic rfa planning, *Lect. Notes Comput. Sci.*, 3750:49–56, 2005.
25. Kapoor, A., Li, M., and Wood, B., Mixed variable optimization for radio frequency ablation planning, *Medical Imaging 2011: Visualization, Image-Guided Procedures, and Modeling*, 7964, March 2011.
26. Chen, C.-C. R., Miga, M. I., and Galloway, R. L., Optimizing electrode placement using finite-element models in radiofrequency ablation treatment planning, *IEEE Trans. Biomed. Eng.*, 56(2):237–245, 2009.
27. Wiener, N., The homogeneous chaos, *Ame. J. Math.*, 60(4):897–936, 1938.
28. Meecham, W. C. and Jeng, D. T., Use of Wiener-Hermite expansion for nearly normal turbulence, *J. Fluid Mech.*, 32:225–249, 1968.
29. Chorin, A. J., Hermite expansions in Monte Carlo computation, *J. Comput. Phys.*, 8:471–482, 1971.
30. Chorin, A. J., Gaussian fields and random flow, *J. Fluid Mech.*, 63:21–32, 1974.
31. Maltz, F. H. and Hitzl, D. L., Variance reduction in Monte Carlo computations using multi-dimensional Hermite polynomials, *J. Comput. Phys.*, 32:345–376, 1979.
32. Deb, M. K., Babuška, I. M., and Oden, J. T., Solutions of stochastic partial differential equations using Galerkin finite element techniques, *Comput. Methods Appl. Mech. Eng.*, 190:6359–6372, 2001.
33. Maître, O. P. L., Reagan, M. T., Najm, H. N., Ghanem, R. G., and Knio, O. M., A stochastic projection method for fluid flow, II, Random process, *J. Comput. Phys.*, 181(1):9–44, 2002.
34. Xiu, D. B. and Karniadakis, G. E., Modeling uncertainty in steady state diffusion problems via generalized polynomial chaos, *Comput. Methods Appl. Mech. Eng.*, 191:4927–4948, 2002.
35. Xiu, D. B. and Karniadakis, G. E., Modeling uncertainty in flow simulations via generalized polynomial chaos, *J. Comput. Phys.*, 187:137–167, 2003.
36. Geneser, S. E., Kirby, R. M., and MacLeod, R. S., Application of stochastic finite element methods to study the sensitivity of ecg forward modeling to organ conductivity, *IEEE Trans. Biomed. Eng.*, 55(1):31–40, 2008.
37. Eiermann, M., Ernst, O. G., and Ullmann, E., Computational aspects of the stochastic finite element method, *Comput. Visual. Sci.*, 10(1):3–15, 2007.
38. Babuška, I., Tempone, R., and Zouraris, G. E., Solving elliptic boundary value problems with uncertain coefficients by the finite element method: the stochastic formulation., *SIAM J. Numer. Anal.*, 42(2):800–825, 2004.
39. Ma, X. and Zabaras, N., An adaptive high-dimensional stochastic model representation technique for the solution of stochastic partial differential equations, *J. Comput. Phys.*, 229:3884–3925, 2010.
40. Wan, X. and Karniadakis, G. E., Multi-element generalized polynomial chaos for arbitrary probability measures, *SIAM J. Sci. Comput.*, 28:901–928, 2006.
41. Foo, J. and Karniadakis, G. E., Multi-element probabilistic collocation method in high dimensions, *J. Comput. Phys.*,

229:1536–1557, 2010.

42. Fletcher, R., *Practical Methods of Optimization*, Wiley, New York, 2000.
43. Wang, J. and Zabaras, N., Hierarchical Bayesian models for inverse problems in heat conduction, *Inverse Problems*, 21:183–206, 2005.
44. Wang, J. and Zabaras, N., Using Bayesian statistics in the estimation of heat source in radiation, *Int. J. Heat Mass Transfer*, 48:15–29, 2005.
45. Wang, J. and Zabaras, N., A Markov random field model to contamination source identification in porous media flow, *Int. J. Heat Mass Transfer*, 49:939–950, 2006.
46. Narayanan, V. A. B. and Zabaras, N., Stochastic inverse heat conduction using a spectral approach, *Int. J. Numer. Methods Eng.*, 60:1569–1593, 2004.
47. Gunzburger, M. D., Lee, H.-C., and Lee, J., Error estimates of stochastic optimal neumann boundary control problems, *SIAM J. Numer. Anal.*, 49(4):1532–1552, 2011.
48. Hou, L. S., Lee, J., and Manouzi, H., Finite element approximations of stochastic optimal control problems constrained by stochastic elliptic PDE, *J. Math. Anal. Appl.*, 384(1):87–103, 2011.
49. Tiesler, H., Kirby, R. M., Xiu, D., and Preusser, T., Stochastic collocation for optimal control problems with stochastic pde constraints, *SIAM J. Optim.*, under review, 2011.
50. Bourquain, H., Schenk, A., Link, F., Preim, B., Prause, G., and Peitgen, H.-O., Hepavision2: A software assistant for preoperative planning in living-related liver transplantation and oncologic liver surgery, *Proc. of CARS*, pp. 341–346, 2002.
51. Haemmerich, D., Chachati, L., Wright, A. S., Mahvi, D. M., Lee Jr, F. T., and Webster, J. G., Hepatic radiofrequency ablation with internally cooled probes: Effect of coolant temperature on lesion size, *IEEE Trans. Biomed. Eng.*, 50(4):493–500, 2003.
52. Pennes, H. H., Analysis of tissue and arterial blood temperatures in a resting forearm, *J. Appl. Physiol.*, 1:93–122, 1948.
53. Jain, R. K., Grantham, F. H., and Gullino, P. M., Blood flow and heat transfer in Walker 256 mammary carcinoma, *J. Natl. Cancer Inst.*, 69:927–931, 1979.
54. Creeze, J. and Lagendijk, J. J. W., Temperature uniformity during hyperthermia: The impact of large vessels, *Phys. Med. Biol.*, 37(6):1321–1337, 1992.
55. Lagendijk, J. J. W., The influence of bloodflow in large vessels on the temperature distribution in hyperthermia, *Phys. Med. Biol.*, 27(1):17–23, 1982.
56. Creeze, J., Mooibroek, J., Lagendijk, J. J. W., and van Leeuwen, G. M. J., The theoretical and experimental evaluation of the heat balance in perfused tissue, *Phys. Med. Biol.*, 39:813–832, 1994.
57. Welp, C., Investigation of the influence of blood flow rate on large vessel cooling in hepatic radiofrequency ablation, *Biomed. Tech. (Berl.)*, 51(5-6):337–346, 2006.
58. Sheu, T. W. H., Chou, C. W., Tsai, S. F., and Liang, P. C., Three-dimensional analysis for radio-frequency ablation of liver tumor with blood perfusion effect, *Comput. Methods Biomech. Biomed. Eng.*, 8(4):229–240, 2005.
59. Arrhenius, S., Über die Reaktionsgeschwindigkeit bei der Inversion von Roherzucker durch Säuren, *Z. Phys. Chem.*, 4:226–248, 1889.
60. Hackbusch, W., *Multi-Grid Methods and Applications*, Vol. 4 of Springer Series in Computational Mathematics, Springer, Berlin, 1985.
61. Keese, A., Numerical solution of systems with stochastic uncertainties: A general purpose framework for stochastic finite elements, PhD Thesis, Technical University Braunschweig, 2004.
62. Kröger, T., Altrogge, I., Konrad, O., Kirby, R. M., and Preusser, T., Estimation of probability density functions for parameters sensitivity analyses, *Proc. SimVis*, pp. 61–74, Magdeburg, 2008.
63. Kaipio, J. and Somersalo, E., Statistical inverse problems: Discretization, model reduction and inverse crimes, *J. Comput. Appl. Math.*, 1098:493–504, 2007.
64. Preusser, T., Liehr, F., Rumpf, M., Sauter, S., Weikard, U., and Peitgen, H.-O., Simulation of radio-frequency ablation using composite finite element methods, *Perspective in Image Guided Surgery*, pp. 303–310, Remagen, 2004.
65. Liehr, F., Preusser, T., Rumpf, M., Sauter, S., and Schwen, L. O., Composite finite elements for 3D image based computing,

Comput. Visual. Sci., 12(4):171–188, April 2009.

66. Pätz, T., Kröger, T., and Preusser, T., Simulation of radiofrequency ablation including water evaporation, In *IFMBE Proc.*, Vol. 25(4), pp. 1287–1290, Springer, Berlin, 2009.
67. Xiu, D. B. and Hesthaven, J. S., High-order collocation methods for differential equations with random inputs, *SIAM J. Sci. Comput.*, 27(3):1118–1139, 2005.